Nuclear Materials and Energy 27 (2021) 100994

Contents lists available at ScienceDirect

Nuclear Materials and Energy

journal homepage: www.elsevier.com/locate/nme

Invited Review

# Data on erosion and hydrogen fuel retention in Beryllium plasma-facing materials

Gregory De Temmerman [a,b,c,*], Kalle Heinola [d], Dmitriy Borodin [e], Sebastijan Brezinsek [e], Russell P. Doerner [f], Marek Rubel [g], Elżbieta Fortuna-Zaleśna [h], Christian Linsmeier [e], Daisuke Nishijima [f], Kai Nordlund [i], Michael Probst [j], Juri Romazanov [e], Elnaz Safi [i], Thomas Schwarz-Selinger [k], Anna Widdowson [l], Bastiaan J. Braams [d,m], Hyun-Kyung Chung [d,n], Christian Hill [d]

[a] ITER Organisation, Route de Vinon-sur-Verdon, CS 90 046, 13067 St. Paul Lez Durance Cedex, France
[b] Zenon Research, 16 rue Séguier, 75006 Paris, France
[c] MINES ParisTech, Université PSL, Institut des Hautes Etudes pour l'Innovation et l'Entrepreneuriat (IHEIE), 75006 Paris, France
[d] International Atomic Energy Agency, A-1400, Vienna, Austria
[e] Forschungszentrum Jülich GmbH, D-52425, Jülich, Germany
[f] Center for Energy Research, University of California, San Diego, La Jolla, CA 92093-0417, USA
[g] KTH Royal Institute of Technology, SE-1044 Stockholm, Sweden
[h] Warsaw University of Technology, 02 507 Warsaw, Poland
[i] Department of Physics, University of Helsinki, P.O. Box 43, 00014 Helsinki, Finland
[j] Institute for Ion Physics and Applied Physics, University of Innsbruck, 6020 Innsbruck, Austria
[k] Max-Planck-Institut für Plasmaphysik, Boltzmannstr. 2, 85748 Garching, Germany
[l] CCFE, Culham Science Centre, Abingdon, OX14 3DB, United Kingdom
[m] Centrum Wiskunde and Informatica, P.O. Box 94079, 1090 GB, Amsterdam, The Netherlands
[n] Korea Institute of Fusion Energy, 169-148 Gwahak-ro, Yuseong-gu, Daejon, 34133, Republic of Korea

ARTICLE INFO

*Keywords:*
Beryllium
Controlled fusion
Plasma-facing material
Erosion–deposition
Dust

ABSTRACT

ITER will use beryllium as a plasma-facing material in the main chamber, covering a total surface area of about 620 m$^2$. Given the importance of beryllium erosion and co-deposition for tritium retention in ITER, significant efforts have been made to understand the behaviour of beryllium under fusion-relevant conditions with high particle and heat loads. This paper provides a comprehensive report on the state of knowledge of beryllium behaviour under fusion-relevant conditions: the erosion mechanisms and their consequences, beryllium migration in JET, fuel retention and dust generation. The paper reviews basic laboratory studies, advanced computer simulations and experience from laboratory plasma experiments in linear simulators of plasma–wall interactions and in controlled fusion devices using beryllium plasma-facing components. A critical assessment of analytical methods and simulation codes used in beryllium studies is given. The overall objective is to review the existing set of data with a broad literature survey and to identify gaps and research needs to broaden the database for ITER.

## 1. Introduction

Beryllium (Be) has been on the list of candidates for plasma-facing materials (PFM) in nuclear fusion devices since the late 1980s. With the decision to use Be as the material for the first wall (FW) in the main chamber of ITER, the research on its fusion-relevant aspects has been accelerated. The properties of Be for fusion applications have been reviewed several times [1–4]. Understanding Be-related plasma–wall interaction (PWI) mechanisms such as the erosion of Be by hydrogen isotope (H, D, T) and impurity particle bombardment as well as the hydrogen isotope inventory in Be and Be-containing materials became a major scientific issue and the topic of numerous studies [5–65]. The influence of neutron-induced defects in Be has also been addressed in specific studies [66–96]. However, since no neutron source with the typical spectrum from D-T fusion reactions is available, those studies rely on defects created by fission neutrons. The fundamental aspects of Be surfaces [97–133] and their behaviour upon hydrogen adsorption

* Corresponding author.
*E-mail address:* greg@zenonresearch.org (G. De Temmerman).

https://doi.org/10.1016/j.nme.2021.100994
Received 30 October 2020; Received in revised form 12 March 2021; Accepted 29 March 2021
Available online 26 April 2021

**Abbreviations**

| | |
|---|---|
| ADAS | atomic data and analysis suite |
| AMS | accelerator mass spectrometry |
| BCA | binary-collision approximation |
| BM | blanket module |
| CAPS | chemically assisted physical sputtering |
| CFC | carbon-fibre component |
| CRM | collisional-radiative model |
| CX | charge-exchange particle |
| DFT | density functional theory |
| EDX | energy dispersive X-ray spectroscopy |
| ELM | plasma edge-localized mode |
| EPMA | electron probe microanalysis |
| ERDA | elastic recoil detection analysis |
| ERO | kinetic Monte Carlo simulation code for erosion |
| FIB | focused ion beam |
| FW | first wall |
| FWP | first wall panel |
| IBA | ion beam analysis |
| ICRH | ion cyclotron radio heating |
| ICWC | ion cyclotron wall conditioning |
| ILW | ITER-Like Wall project at JET |
| IP | image plate technique |
| IWC | inner wall cladding |
| IWGL | inner wall guard limiter |
| JET | Joint European Torus |
| JET-C | JET with full carbon wall |
| JET-ILW | JET with all metal ITER-Like Wall |
| LIBS | laser-induced breakdown spectroscopy |
| LID | laser-induced desorption |
| LSC | liquid scintillation counting |
| MD | molecular dynamics |
| MS | metastable state |
| NRA | nuclear reaction analysis |
| NRADC | NRA deconvolution suite |
| OES | optical emission spectroscopy |
| OKMC | object kinetic Monte Carlo |
| OSM | onion skin model |
| PDE | partial differential equation |
| PEC | photon efficiency coefficient |
| PFC | plasma-facing component |
| PFM | plasma-facing material |
| PFS | plasma-facing surface |
| PIXE | particle-induced X-ray emission |
| PSI | plasma-surface interaction |
| PWI | plasma–wall interaction |
| qMS | quasi-metastable state |
| QMB | quartz microbalance |
| RBS | Rutherford backscattering spectrometry |
| RH | remote handling |
| SEM | scanning electron microscopy |
| SIMS | secondary ion mass spectrometry |
| STEM | scanning variant of TEM |
| SOL | scrape-off layer |
| SOLPS | scrape-off layer plasma simulation code |
| TDS | thermal desorption spectrometry |
| TEM | transmission electron microscopy |
| TMAP | tritium migration and permeation code |
| TPE | tritium plasma experiment |
| TRIM | transport of ions in matter code |
| UDP | upper dump plate |
| WallDYN | plasma–wall dynamics code |
| XPS | X-ray photoelectron spectroscopy |
| XRD | X-ray diffraction spectroscopy |

with respect to surface structure and reconstruction have been studied both experimentally and by ab initio methods [134–142].

Be has been used in plasma-facing components (PFCs) of several fusion devices, including as test limiters in UNITOR [143] and ISX-B [144,145], thin layers by in vacuo evaporation in the Joint European Torus (JET), divertor material in JET during 1994–1995 campaigns and eventually as material for the limiters and cladding in the main chamber of JET with the JET ITER-Like Wall (JET-ILW) project [146]. In addition to the relatively high melting point of Be (1560 K), other properties attractive for the PFMs of fusion devices include (i) a low atomic number ($Z = 4$) ensuring good plasma compatibility by minimizing the radiation losses associated with Be penetrating in the core plasma [147], (ii) high thermal conductivity (~200 $Wm^{-1}K^{-1}$ at room temperature) (iii) high reactivity with oxygen making it a good getter material. In JET-ILW, Be is acting intrinsically as low-$Z$ conditioning species comparable to other low-$Z$ species like lithium (Li) or boron (B) which must be extrinsic, applied by Li-evaporation or boronisation before or during plasma-operation. No additional low-$Z$ conditioning is therefore required in JET-ILW or in ITER.

As a drawback, the low atomic mass implies relatively efficient plasma-surface interaction (PSI) processes, such as sputtering by plasma particles as discussed in Section 3.2 below. Originally, Be was also expected to have a low hydrogen retention rate as compared to retention in carbon (C) because of the absence of chemical interactions between Be and H. While the retention is indeed lower than that of C-based materials, there is evidence for complex chemical interactions involving Be and H with the formation of molecular compounds. This point will be discussed in Sections 3.3, 5.2 and 6.2 . However, even though Be layers are formed due to Be erosion followed by deposition in the main chamber and in the divertor [148], the fuel content in these Be layers is significantly lower than in C layers which have been built up under comparable surface temperature and impinging flux conditions [149]. The erosion processes and migration will be presented in Section 5.

Nevertheless, the application of Be in fusion devices has been limited to the mentioned toroidal devices because of health hazards related to its toxicity, especially in the form of Be oxide dust [150]. Dedicated safety precautions during the installation, operation and removal of components are required [151]. Another, less major, issue is the activation of $^{9}Be$ (the only stable Be isotope) under neutron flux to $^{10}Be$, which has a half-life of $t_{1/2} = 1.39 \times 10^{6}$ y.

This paper provides a comprehensive report on the state of knowledge of Be behaviour under fusion-relevant conditions: erosion mechanisms and their consequences, migration of species, fuel retention and dust generation. Processes related to Be activation in fusion devices have been discussed previously elsewhere [152]. The overall objective is to present an existing set of data with a broad literature survey and to identify gaps and research needs to broaden the database for ITER.

## 2. Beryllium in ITER

Plasma-facing components (PFC) made of Be will be used in the main chamber of ITER where the total surface area covered with Be will be about 620 $m^2$ [153] for a total mass of about 12 tons. Since the

material combination planned for ITER [154], Be first wall (FW) and W divertor, had never been tested in a tokamak, the JET-ILW project was initiated in 2004 [155] to study the compatibility of plasma operations with the ITER material mix and to quantify the fuel retention and material migration in such a configuration. The material configuration of JET was changed from a first wall and divertor made of carbon-fibre enforced composites (CFC) to a configuration with a full-W divertor and with Be components in the main chamber wall: bulk metal Be inner and outer limiters and upper dump plates (UDP), and Be coatings on the inner wall cladding (IWC) tiles. An overview of the observations related to retention and migration can be found in Ref. [64]. The underlying physical processes for Be erosion at the JET main chamber by impinging hydrogen isotope ions, energetic hydrogen isotope neutrals as well as Be ions will be described in the upcoming sections.

The ITER blanket First Wall (Fig. 1) faces the plasma directly and is made of 440 blanket modules (BMs), each comprised of a plasma-facing FW panel (FWP) and a shield block made of stainless steel (316L(N)-IG). A detailed description of the ITER blanket design can be found in Ref. [153]. The BMs are segmented into 18 poloidal sections, for a total of 440 BMs inside the machine. The typical size of a BM is about 1 m × 1.4 m × 0.5 m. The BMs are actively cooled by water (inlet temperature 70 °C, inlet pressure 4 MPa, total heat removal capacity up to 736 MW). Two types of FWP exist, depending on the expected steady-state heat loads. Two types of cooling technologies were retained for the FWP: a "normal heat flux" technology rated for up to 2 MW m$^{-2}$ and an "enhanced heat flux technology" capable of up to 4.7 MW m$^{-2}$ [156]. The plasma-facing units are made of "fingers" whose design differs for the two types of FWP: SS316L(N)-IG tubes for normal heat flux FW panels, in which the SS tubes are embedded into a copper alloy (CuCrZr); and hypervapotron channels made of CuCrZr alloy for enhanced heat flux FW panels. The Be armour thickness will be about 8–10 mm.

Because of the shaping of the panels, the heat and particle loading on the FW will be strongly inhomogeneous; an illustration of this can be found in Ref. [157]. The FWPs will be subject to bombardment by plasma particles, both plasma ions and energetic charge-exchange (CX) neutrals, the energy and magnitude of which will define the amount of erosion/deposition in the device. Computer simulations are required to determine the stationary heat loads on components. These have been done with plasma fluid simulations using the SOLPS code. Simulations have been mainly performed in 2D and therefore do not account for the 3D nature of the wall, however, 3D edge plasma codes are now becoming available. The SOLPS numerical grid does not extend to the main wall, and extrapolations have been made using the Onion-Skin Model (OSM) fluid code based on different considerations from the ITER Heat and Nuclear Load Specifications [158]. Details of this procedure can be found in Refs. [159,160]. Fig. 2 shows typical poloidal D flux profiles for two extreme cases of a low and high density scrape-off layer (SOL) plasma for a Q = 10 ITER burning plasma assuming full 2D symmetry. The particle flux on the FW is orders of magnitude lower than in the divertor, but can still be of the order of $10^{20} - 10^{21}$ m$^{-2}$s$^{-1}$. The areas of most intense interactions are on BM-5 because of the small distance between the plasma and the inner wall [161], near the top of the machine (BM-8 and 9) in the vicinity of the secondary X-point [158] and on BM-11 and BM-18 where the second separatrix intersects with the wall [162]. The CX neutral particle energy can be relatively high because of the high pedestal temperature in ITER ($T_{e,ped} \sim 5$ keV). The global Be erosion, transport and deposition in the full ITER vessel geometry has been modelled by the 2D version of the WallDYN code [163] and in the most advanced, fully parallelized 3D Monte-Carlo Code ERO2.0 [164] for the steady-state phase of various ITER plasma backgrounds from SOLPS . The heat loads induced by plasma edge-localized modes (ELMs) on the FW have been evaluated in Ref. [165] for a global ELM-induced energy drop of the plasma by 0.6 MJ. Only a fraction of this goes to the FW so the 0.6 MJ corresponds to the maximum ELM size for surface melting or significant evaporation avoidance in the divertor [166]. However, high ELM frequency (>30–50 Hz) will result in Be surfaces being exposed to a large number of transient heating cycles which could lead to significant roughening/cracking of the surface [167]. Significant surface melting could occur during disruptions as discussed in Refs. [168–170].

## 3. Fundamental data for erosion, deposition, hydrogen isotope retention

Erosion is the term used to describe the fundamental processes by which energetic particles remove atoms from a plasma-facing surface (PFS). The most straightforward erosion diagnostic, for an elementally pure material, is measuring the mass change of a sample. Another technique useful in a plasma environment involves spectroscopically measuring the photons emitted by eroded atoms that are excited by the plasma, as is described later in Section 4.2.

Physical processes typically listed under the heading of Be erosion include: physical sputtering, chemically-assisted physical sputtering and thermally induced release of material, i.e. sublimation, evaporation, and melting accompanied by splashing. The other process associated with erosion is chemical erosion, where volatile species formed chemically on the surface are released e.g. by thermal activation, but this process has not been detected with Be samples.

Hydrogen retention in PFCs takes place as the hydrogen enters the bulk through the surface and gets immobilized or trapped in some lattice defect in the material, such as impurities, vacancies and other open-volume defects, grain boundaries, and other imperfections. Retained hydrogen increases the hydrogen inventory in material which in turn has an influence on the material's functionality as a PFM. The material's ability to recycle hydrogen fuel back to plasma gets inhibited, and the material's physical properties may be altered through embrittlement. Further, retained and immobilized tritium is a radiological hazard, and therefore a safety concern. Hence, understanding retention and its underlying mechanisms is of crucial importance and an active field in PFC materials research today.

Methodologies used to quantify Be erosion and deposition as well as hydrogen retention in Be will be discussed in Section 3.1. Details on Be erosion processes and on retention will be given in Sections 3.2 and 3.3, respectively.

### 3.1. Experimental methodologies for fundamental research

Experimental analysis methods can be used for hydrogen isotope and other elemental impurity quantification and depth profiling, such as thermal desorption spectrometry (TDS), secondary ion mass spectrometry (SIMS), high energy ion beam analysis methods including Rutherford backscattering spectrometry (RBS), nuclear reaction analysis (NRA) and elastic recoil detection analysis (ERDA), and various laser-based methods. These methods combined allow detailed research on hydrogen trapping and transport in materials and have been applied for material sputtering, erosion and deposition studies as well. Each experimental technique has its own advantages and disadvantages, which are outlined in the following paragraphs.

Analyses performed with TDS are standard for measuring the total amount of hydrogen in a given sample. By heating the samples with a controlled temperature ramp and simultaneously measuring the released volatile species it is possible to quantify the absolute amount of all hydrogen isotopes and, by repeating the measurements with identical samples but different heating rates, it is possible to gain insight into the binding and activation energies of the trapping, detrapping and diffusion processes in the material (Section 6.2.2). Using SIMS all hydrogen isotopes and other impurities can be detected. It has good depth resolution [171], but the results are hard to quantify absolutely and may be prone to matrix effects. Also NRA can be used for any hydrogen isotope detection [172], but in practice limitations are often encountered since not all facilities are licenced to operate

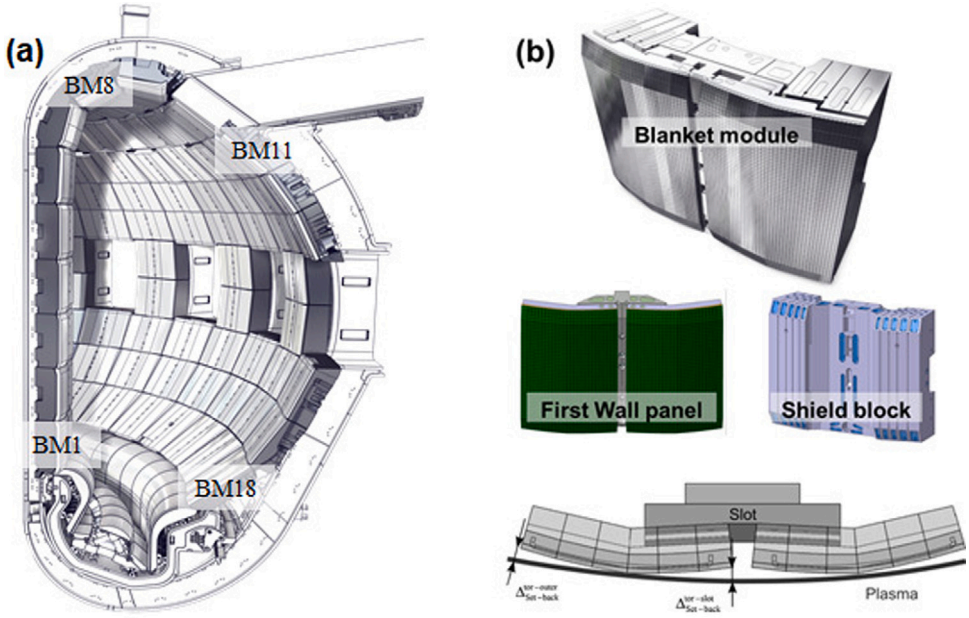


**Fig. 1.** (a) Cut-away of the ITER vacuum vessel illustrating the Be first wall and tungsten divertor. (b) Schematic view of a blanket module made of a plasma-facing first wall panel and a shield block. The FW panels are shaped to shadow the remote handling access holes and avoid possible leading edges in the case of radial misalignment between adjacent FWPs. The blanket modules are numbered from 1 (inboard side) to 18 (outboard side).
*Source:* Reproduction from Ref. [153].

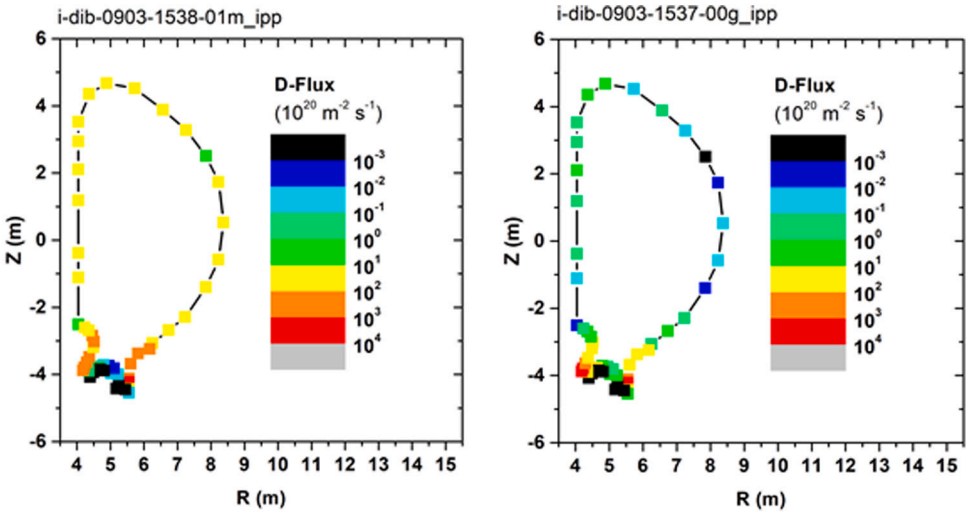


**Fig. 2.** Poloidal distribution of D fluxes in ITER for two assumptions on the far-SOL density profiles (left) high density, and (right) low density.

with all, often radioactive, projectile species, and not all set-ups have the necessary detectors to analyse gamma photons. NRA can be applied for detecting Be and other fusion-relevant light impurities, such as O and C. Cross section data required for detecting Be with NRA are very scarce, but the increasing requirement in fusion materials research has recently induced new reaction cross sections [173–175]. For depth profiling of hydrogen isotopes in Be the main reactions are: for protium p($^{15}$N, $\alpha\gamma$)$^{12}$C, for deuterium D($^{3}$He, $\alpha$)p [144,176,177], and for tritium T($^{12}$C,p)$^{14}$C and T($^{12}$C, $\alpha$)$^{11}$B [178]. However, ERDA can be applied more efficiently for T depth profiling and quantification due to ERDA sensitivity for T when using low energy $^{4}$He beams (see e.g. Refs [172,179–182]). Also, a highly sensitive method, so-called accelerator mass spectrometry (AMS), has been recently applied for T depth profiling with a triton detection limit of $10^{11}$ Tm$^{-3}$ and up to a depth of 25 μm [183].

ERDA is based on the direct detection of recoils from the samples. The technique can be used for depth profiling of all hydrogen isotopes and other impurities. Due to the grazing incidence of the primary ion beam, the method is usually restricted to smooth sample surfaces and the analyzable depth is usually small compared to ion beam methods with more perpendicular incidence such as RBS or NRA. However, for suitable samples, profiles with exceptionally good depth resolution can be achieved by ERDA. As an example, in Ref. [184] an analyzable depth of $< 0.5$ μm with a hydrogen depth resolution of 80 nm was obtained for $^{7}$Li-ERDA on a-C:H films.

For NRA, data analysis is typically performed using maximum likelihood approaches, e.g. with the Nuclear Reaction Analysis DeConvolution (NRADC) software [185]. In Ref. [186] it was shown that the achievable depth resolutions calculated from NRADC and conventional forward calculations agree and are ~100 nm for near-surface D and 1.6 μm for D layers in the depth of 8 μm W. A study directly dedicated for depth profiling of D in Be [176] showed that by using both $\alpha$-particles and protons from the D($^{3}$He, $\alpha$)p reaction, a depth resolution of 140 nm for near-surface D in Be can be achieved, but

an optimized $^{28}$Si-ERDA can reach a depth resolution of better than 50 nm. A novel approach, called total-IBA, of combining simultaneous analysis of results obtained from the measurements of D and other impurities in Be using RBS, NRA and particle-induced X-ray emission (PIXE) has been recently developed [65,187]. In total-IBA, the results from multiple measurement techniques are analysed in parallel using the Bayesian data furnace method, making it suitable for large-scale analyses of fusion PFCs, such as JET-ILW (see Refs. [65,188–191] and Section 5.1.2).

For the laser-based methods many different names for methodologies with overlapping analysis regimes and techniques exist. They can be mainly differentiated by the duration of the laser pulse, ranging from femtosecond to millisecond, the laser energy density, and the observed species (photons or particles) [192]. The depth profiles measured with laser-induced breakdown spectroscopy (LIBS) agree qualitatively with those measured by SIMS. For a LIBS system with a 5-ns Nd:YAG laser (pulse energies up to 650 mJ at 1064 nm), ablation depths of 100–2500 nm per laser pulse are reported in Be-containing layers from the JET-ILW [193]. One challenge with LIBS hydrogen depth profiling is that for millisecond and nanosecond pulse lengths, the heat penetration depth is larger than the ablation depth per pulse and therefore hydrogen can desorb from regions deeper in the sample. This can be overcome by the use of femtosecond laser pulses [194]. LIBS in the picosecond domain delivers, therefore, the best compromise by minimal thermal interaction with the bulk material and good sensitivity with respect to the hydrogen isotope quantification with a typical depth resolution of ~100 nm and a typical spot size of ~1 mm. Laser-induced desorption (LID) spectroscopy is a technique to quantify trapped hydrogen isotopes by locally heating the samples with a laser and to observe spectroscopically the fuel emission. It is also possible to measure the released fuel with gas analysis utilizing mass spectrometry. This technique is labelled as LID-QMS and tritium-compatable systems have been recently installed and tested in Ref. [195], and it is foreseen as an in-vessel technique to be used in ITER. The power density and pulse duration applied in LID should be chosen so that the pulse-induced thermal heating of the sample is sufficient to release all hydrogen in a single pulse, but not to induce melting or significant sublimation of the bulk material. It should be mentioned that full release of hydrogen fuel only occurs when the temperature approaches the melting temperature of Be [195,196]. While the method is already widely established on fusion materials, measurements on Be-based materials are still rare [196], but detailed studies were recently performed on bulk Be and on Be layers [195] demonstrating full desorption of fuel from these samples.

### 3.2. Sputtering and erosion of beryllium

#### 3.2.1. Sputter yields of beryllium in ion beam experiments

Physical sputtering occurs when an energetic particle, either neutral or charged, transfers sufficient energy to lattice atoms in the sample to overcome the surface binding energy of the material. The result is the ejection of atoms from the surface of the material. Due to the surface binding energy of Be, 3.38 eV, the released Be atoms have a large velocity and can travel a significant distance before becoming ionized by any nearby plasma. Physical sputtering is typically well described by binary-collision models of the interactions [197] and such models have been validated under certain conditions using ion beam bombardment experiments [198] of Be targets.

Early ion beam experiments have provided the best grounds to establish the data based on physical sputter yields of many target materials by particle impact. The advantage of ion beams over plasma experiments are manifold. First, the flux of particles hitting the target under investigation can be measured directly and with higher accuracy than for plasma experiments. Generally, this is done by measuring the current collected at the sample position with so-called Faraday cups. Secondary electrons created by the impacting ion can be suppressed by a careful design of geometry or by the use of biased apertures in front of the sample. Measuring the lateral flux distribution or scanning the focused beam over the surface further reduces the error bar in the flux determination down to a few percent. Secondly, the energy can be easily set by the extraction potential. Taking into account that the energy spread in the ion source is at most in the few eV range and extraction potentials are typically in the keV range, ion beams can be considered mono-energetic and have a narrow emittance. In contrast to experiments with plasma devices, mass separation can be easily achieved by a bending magnet and hence beams of atomic or specific molecular ions can be generated free of impurities, which is a prerequisite to compare results with modelling. Finally, by tilting the substrate, the angle of incidence of the beam can be easily changed and measurements as function of angle of incidence can be performed.

However, there are also obvious drawbacks of ion beam experiments. First, fluxes that can be reached are only in the $10^{18} - 10^{19}$ ions $m^{-2}s^{-1}$ range, which is at least one to two orders of magnitude less than expected for the FW in ITER (see Section 2). Hydrogen isotope solute concentrations in the Be lattice are therefore smaller and possible effects that prevail in plasma experiments cannot be addressed with ion beams. Also, sputter yield measurements at low energies are barely accessible because due to space charge limitations, the flux density at the target drops even further for lower ion energies. This is most serious for Be data as the sputtering threshold for this very light metal is much smaller than for heavier metals. Due to the efficient energy transfer in collisions of light ions with Be, the threshold for physical sputtering is low (e.g. for deuterium and perpendicular angle of incidence, 9.5 eV).

Even if experiments are conducted successfully at low energies, the results become less reliable for several reasons. Experimental data below 100 eV may be too large due to the non-negligible energy spread and the angular divergence of the incident beam [199]. In addition, energetic neutrals that are created by charge exchange collisions in the beam path can affect the results because extraction is typically done in the keV range and particles are decelerated only directly in front of the target to minimize particle losses on the flight path. Next, for low energies and hence low fluxes, oxidation has to be considered for reactive materials such as Be. In Ref. [6] a $D_3^+$ ion beam was used to study Be sputtering, but due to the low ion flux used, the low sputter yield and the efficient O gettering of Be surfaces, the results obtained may represent D retention feature in BeO rather than D-induced Be sputtering. To conclude, the D adsorption rate to oxygen-containing species in the sample must be smaller than the erosion rate, which is defined by the arrival rate of the D ions multiplied with the sputter yield. This can be highlighted with the following example. Assuming a sticking probability to oxygen of unity, a D flux of $2 \times 10^{19}$ $m^{-2}s^{-1}$ and taking the sputter yield for BeO to be 0.01 at a D energy of 200 eV into account, one gets a partial pressure for oxygen of $4 \times 10^{-8}$ mbar (or $3 \times 10^{-8}$ mbar for water) where both effects balance each other. For such conditions, sputter yield measurements of clean Be samples yielded those values obtained for BeO [200] (Fig. 3). Only at elevated temperatures (T > 650 °C) is Be assumed to diffuse through the oxide layer enabling the sputter yield of clean Be to be measured reliably [200,201].

Another drawback of Be sputter experiments with light ions is the formation of surface roughness. As was shown in Ref. [202] when eroding Be with hydrogen ions, a needle-like surface roughness evolved that lowered the Be sputter yield. The cause for this roughness evolution is assumed to be the lower sputter yield range for nearly all possible surface impurities, such as C, N or any metal, and occurs with surface oxides as well as with clean Be. As a consequence, the surface will be enriched with impurity species, leading to surface roughening which in turn modifies the sputter yield. The latter was shown for Be in Ref. [203], where the sputter yield was measured as a function of angle of incidence for H erosion of Be together with the surface morphology. In that case the erosion yields at normal incidence were increased as compared to a perfectly flat surface, while they were observed to reduce at glancing angles.

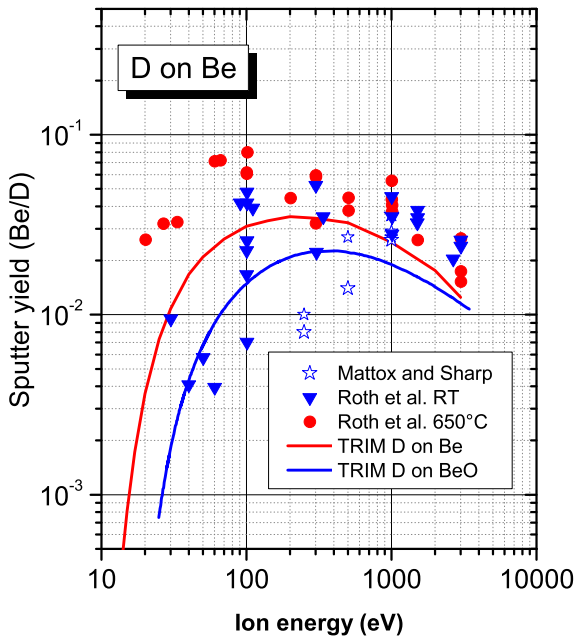


**Fig. 3.** Experimental sputter yields of D on Be obtained by Mattox and Sharp [202], and by Roth [200] in comparison with BCA calculations using TRIM. The impact energies are mono-energetic and the impact angle is perpendicular to the mirror-like surface.

In summary, the database on Be sputter yields derived from ion beam experiments is much less sound than for most other metals, especially for light ion bombardment. Sputter yields of Be with heavier ions such as Ne, Ar and Xe are considered much more reliable as some of the challenges that exist for light ion bombardment are less critical. Due to the higher sputter yield, oxidation is substantially reduced. Likewise, heavier impurities are sputtered more effectively and surface roughness is not expected to evolve. In that sense they are also a test case to compare with binary collision approximation (BCA) simulations and the agreement is satisfying. The erosion rates of Be, BeO, $Be_2C$, and $Be_4B$ due to ion bombardment were reviewed in Ref. [201]. Fig. 3 presents D-induced experimental Be and BeO sputtering rates compared with computational rates obtained with BCA. The Be sputtering yield values obtained experimentally and by computer simulations for pure Be with H, D, T, He, Be, C, O, Ne, and Ar bombardment together with parameters for fit formulae to calculate sputter yields as function of projectile energy and angle of incidence are compiled in Ref. [204].

### 3.2.2. *Beryllium erosion in plasma experiments*

Measuring physical sputtering in a high flux plasma environment with high fluences ($>10^{21}$ ions $cm^{-2}$) is somewhat more complex as compared to ion beam experiments (see Section 3.2.1). The one simplifying factor is that in most high flux plasma devices the ion flux to the surface is sufficiently large to remove the native oxide layer very quickly on the initiation of the plasma bombardment [205]. Complicating factors involved in plasma-based measurements include issues of quantitatively determining the plasma species interacting with the surface. This can include plasma impurity ions, multiply charged ions in the plasma and molecular ion species [206]. In plasma confinement facilities, the ion flux is usually characterized by a Maxwellian energy distribution, or a temperature distribution. Detailed modelling of the PSI processes must include this energy distribution of the impinging ions (relevant, for example, for sputtering threshold studies); this makes a comparison with BCA data more complex.

Linear plasma devices offer a simpler environment to measure sputtering due to plasma bombardment. In such devices the ion temperature in the plasma is usually only a few eV and the incident energy of the ions interacting with the surface is obtained by biasing the targets negatively. In principle, this allows for an almost mono-energetic ion energy distribution (within an eV or two) measurement of physical sputtering. In practice, however, one must still be concerned with multiply charged ion species, impurities and molecular ions contained in the plasma. Due to the potential drop near the surface of the targets, multiply-charged ions interact with the surface with increased energy compared to a singly charged ion. On the other hand molecular ions (such as $H_2^+$ and $H_3^+$) interacting with the surface is equivalent to twice the flux of $H^+$ ions and one half the energy ($H_2^+$), or three times the $H^+$ flux at one third the energy ($H_3^+$) based on the assumption that the molecule kinetic energy greatly exceeds the molecule binding energy (e.g. for $H_2$ the binding energy is 4.748 eV). Taking into account these complications, the physical sputtering rate measured in high flux plasma devices is lower than that measured in lower-flux ion beam devices. For hydrogenic, or helium, plasma incident on Be this is typically smaller by a factor of 5–10 [207].

In co-deposition studies conducted on the Tritium Plasma Experiment (TPE) device [208], the erosion yield was not mentioned in publications, however the measured yield was also lower than calculated TRIM values [209]. This can be seen by using the details of the plasma exposure conditions and geometry mentioned in Ref. [208]. When the TRIM calculated value for Be erosion by 100 eV deuterium ions is used (i.e. $3\times10^{-2}$ atoms/ion) along with the geometry specified in Ref. [208] one expects to measure a co-deposited Be layer thickness of approximately 650 nm. After the experiment was complete, Nuclear Reaction Analysis (NRA) determined the layer thickness to be only 150 nm. Also in Ref. [208], an additional co-deposition experiment using an incident flux 3 times higher, resulted in a layer thickness increase of only a factor of 2. These measurements are consistent with a reduction of erosion yield with increasing ion flux to the target. Similar reduced Be erosion rates have been observed in high flux plasma confinement experiments at PISCES-B [210]. Reduced erosion yields of other materials have also been documented when subjected to high flux plasma bombardment [211].

Part of the explanation for this reduction appears to be related to the development of morphology on the surface of the Be targets [202]. That is, an increase of the surface roughness in comparison to smooth or polished surfaces. As shown in Section 3.2.1, a similar cone-like morphology, and the resulting reduction of erosion due to the cones, has also been observed in high flux ion beam irradiation of Be surfaces [205]. Unfortunately, this reduction of physical sputtering is typically only a factor of 2–3 for Be surfaces that do not exhibit surface impurity deposition during the plasma exposure [205]. Another factor must come into play, further reducing physical sputtering during high flux bombardment of surfaces.

It is speculated that the high incident flux of ions results in a large quantity of plasma species atoms becoming embedded in the near surface of the plasma exposed targets. Soon after the plasma bombardment of the target begins, a steady-state situation is established by the concentration of gas atoms in the surface increasing until release from the surface balances the incoming flux of ions. The time taken to reach this equilibrium obviously depends on the ion flux. In the simplest view, a concentration of 50% gas atoms incorporated in the surface would dilute the concentration of target atoms in the surface and result in a factor of 2 reduction of physical sputtering. Similarly, a 66% concentration of gas atoms would reduce physical sputtering by a factor of 3. Of course, gas atoms do more than just reduce the surface concentration of metallic atoms. Gas atoms in the surface can form chemical bonds with the metallic lattice atoms and change the surface binding energy, thereby altering the physical sputtering from the surface. While attempts have been made to simulate the role of gas atoms on physical sputtering [212], to date there have been no measurements of the actual concentration of gas atoms in the surface during plasma exposure, so the theories remain unproven.

The formation of chemical bonds between hydrogenic gas atoms and Be atoms near the surface has another effect on sputtering. The presence of such bonds can promote a process referred to as chemically assisted physical sputtering (CAPS) [213], which is also known as swift chemical sputtering [214]. This process has been observed in JET [215] and extensively studied experimentally in PISCES-B [216,217] and results in the sputtering of a radical BeH, or BeD, molecule from the plasma-exposed surface. Formation of BeT can be expected similarly to take place with T-containing plasmas. The process involves an incoming ion disrupting, or breaking, a bond in the surface that supplies sufficient energy to a BeH, BeD or BeT molecule and causes it to be energetically released, or sputtered, from the target. This process has been modelled for BeD [218] and the predictions of the model subsequently verified by experiments in PISCES-B [216] and JET [213]. At low incident ion energy, the release of BeD is the dominant material loss channel, but at higher energy physical sputtering is dominant [218]. The process exhibits a surface temperature dependence that causes it to be reduced during higher surface temperature operation. An open question persists as to the sputtering of $BeD_2$ (the stable form of the Be deuteride molecule) from the surface; since its signature emission would be expected deep in the infrared wavelengths, experimental measurements have not been possible so far.

### 3.3. Hydrogen retention in plasma experiments

#### 3.3.1. Hydrogen retention in bulk Be

Deuterium retention in Be surfaces due to low energy ion bombardment, which is typical of plasma exposure, shows a clear saturation with increasing fluence [219]. The saturation is believed to result from an over-saturation of deuterium near the surface of the Be which results in the formation of small gas filled bubbles. At high enough fluence, these gas bubbles appear to grow and interconnect and thereby allow pathways back out of the sample for implanted deuterium ions [29]. The magnitude of the retention depends on other factors, such as temperature and ion energy, but is typically in the $10^{20}$ $Dm^{-2}$ range (Ref. [219] and references therein) and any release above 923 K is negligible [15]. The temperature dependence of D retention in Be was also extensively covered in Ref. [219]. The observed saturation of the H retention is attributed to the formation of the interconnected bubbles, which prevent deep diffusion into the bulk.

It has been documented that impurities in a plasma that can form deposits on the surface (such as C) can drastically increase the retention in Be samples [220]. However, it should be realized that such measurements are not really measurements of retention in Be, but rather a measurements of the retention in the impurity surface coating that forms on the Be sample during the plasma exposure.

#### 3.3.2. Retention in Be co-deposits

Co-deposition of fuel species and Be is predicted to be the primary channel for tritium accumulation within the ITER vacuum vessel [221]. A scaling law has been developed [149] to allow prediction of the D/Be, and hence the T/Be, content ratios in co-deposits. The variables influencing retention were the temperature at which the co-deposit forms, the incident energy of the particles and the deposition rate of the material. The scaling was successfully applied to Be co-deposits formed at a variety of laboratory facilities as follows.

Comparing the results from laboratory facilities to co-deposits formed in the JET-ILW is challenging. Post-mortem analysis has been used to determine the amount of D, Be and other impurities in co-deposits [65,191,222], but these are cumulative campaign values and the conditions where the co-deposits are forming may change shot-to-shot, or day-to-day during the plasma operations. However, knowledge of the locations where co-deposits form can be used to validate material migration codes to allow predictions of where co-deposits are likely to form in ITER. The WallDYN code has been successfully applied to the JET-C and JET-ILW materials and geometry [163]. These results add confidence to the extrapolated predictions of co-deposition and retention rates now used for ITER [163].

Perhaps equally important as being able to accurately predict the amount and location where co-deposits are likely to form in ITER, is the ability to develop efficient techniques to remove the trapped T from co-deposits [223]. Presently, the primary tritium recovery mechanism envisioned for ITER is baking the vessel and divertor to 513 K (240 °C) and 623 K (350 °C), respectively [224]. Deuterium release from Be co-deposits prepared in laboratory conditions has been investigated and successfully modelled under a variety of conditions, including thickness, rate of temperature change, baking time, etc. [225,226].

A further complicating factor for removal of tritium from co-deposits in ITER is the fact that the co-deposits formed during plasma operation have multi-layered structures. Initial experiments to study the influence of successive baking/co-deposition cycles showed that in the case where a fresh co-deposit is formed on top of a partially depleted layer (from a previous bake), the outgassing of the fresh co-deposit will be affected by the depleted under-layers [227]. Later experiments [228] showed that this effect would actually be less important than initially thought because of the annealing of existing traps during the bake.

The effects of adding He ions to the particle flux to bulk Be surfaces, to better simulate the environment of a burning plasma, has also been investigated. The addition of small amounts of He to a D plasma does not change the sputtering yield of bulk Be significantly [229], so the material source term for co-deposition does not change. The influence of He on the D retention in bulk Be targets exposed to the mixed D/He plasma appears to be a small reduction in retention at sample temperatures up to 473 K [229]. Above this temperature, He appears to have no effect. Similarly, a small reduction in retention in Be co-deposits formed during mixed D/He plasma exposure is also observed [230]. Again, as the co-deposition temperature increases the effect disappears. The data from TDS analysis of both D and He exposed bulk Be targets [229,231] and Be co-deposits [230] shows no drastic alteration of the trap energies, as compared to pure D plasma exposure.

Small bubbles have been observed to form in co-deposits of PISCES-B with the presence of He plasmas [232]. Investigations of co-deposits removed from the JET-ILW have also revealed the presence of microscopic bubbles, however, JET-ILW has not been operated with He meaning that these co-deposit bubbles are induced by the hydrogen plasma operations [233,234]. Furthermore, similar bubbles have been observed in the minuscule amounts of dust collected from the JET-ILW (Section 5.3). It is expected that these bubbles increase the fuel retention in co-deposits, but detailed experiments are still needed to quantify the effect.

#### 3.3.3. Hydrogen retention and release in mixed Be-rich materials

Deuterium retention and release behaviour of Be mixed materials have been investigated in order to assess the tritium removal with the wall baking procedure currently suggested for ITER [235–237]. Be samples containing C and W were prepared by the thermal vacuum arc deposition technique [238]. Different strategies were applied for film growth. In one approach, mixed layers with varying Be concentrations were prepared by simultaneously operating one source with Be while a second source was operated with W or C [239]. As the substrate temperature was below 425 K, Be is expected to prevail in metallic form (and C and W are expected to be in the dispersed atomic form).

In another approach, Be alloys were prepared by annealing thin vacuum arc deposited W or C films on Be substrates. From the measured stoichiometry $Be_2C$ and $Be_{12}W$ were deduced to be the dominant phases respectively. Mixed layers of Be/O were prepared by depositing Be layers under a controlled oxygen atmosphere. Deuterium was implanted with a mass-selected $D_3^+$ ion beam with an ion energy of 600 eV (corresponding to an energy of 200 eV $D^{-1}$) at a low flux of $3\times10^{19}$ D $m^{-2}s^{-1}$ to fluences of up to $4\times10^{23}$ D $m^{-2}$. Implantation was conducted for temperatures of up to 570 K. Measured D concentrations

were not significantly different for pure Be, BeO and small additions of C. However, 6 at.% of W reduced the maximum D concentration by a factor of three. Deuterium concentrations decreased with the D irradiation temperature in all cases, except for the Be/C layer with high concentration which showed a more or less constant maximum D concentration value over the investigated temperature range. The decrease with temperature was similar for these ion-implanted thin films to that observed for co-deposited layers grown in PISCES-B plasmas [240]. Besides affecting the level of D retention, mixing the ratio of W or C to Be changed the D desorption behaviour causing less efficient D removal during baking. For the Be–W mixture as well as for the W alloy, D release is still dominated by the low-temperature desorption peak, although its intensity is attenuated compared to the higher-temperature peaks. This is also the case for the $Be_2C$ and the low concentration C mixture (8 at.%). However, for the high C concentrations (50 at.%) D release is dominated by a high temperature peak, characteristic for C–D bonds, which prevents removal of the retained D by baking at 623 K in this case. As a consequence, based on these results, the baking operation in ITER for tritium removal is expected to be efficient for the first wall and Be-rich co-deposited layers formed at low temperature, while it is expected to be inefficient for C-rich co-deposited layers (and also of course for PFS which experience temperatures above 623 K during a discharge).

Recent TDS results obtained with annealing at ITER-baking temperatures, using tokamak samples retrieved from the JET-ILW main chamber bulk Be limiters and from the Be deposits of the W divertor, showed significant remaining D retention after 15 hrs of annealing at ITER-baking temperatures of 513 K and 623 K, respectively [222]. The thickest deposits were found in the divertor area, mostly as a layered sandwich-like structure, and having varying compositions of Be-D-O-C mixtures [191]. The D retention in the divertor deposit samples was found to correlate with the deposit thickness, and the thickest deposits are found on the upper part of the inner divertor (approximate deposit Be:D:O:C ratio 1:0.05:0.07:0.03 after one year JET-ILW campaign in 2013–2014). In the TDS experiments, after 15 hrs annealing at 623 K, the highest remaining D fractions of 54 and 87% were recorded with deposition thicknesses 10 and 40 μm, respectively. All the W divertor samples studied were from the plasma SOL regions, where the fuel retention takes place via co-deposition and low-energy implantation. However, the bulk Be limiter samples analysed were from the limiter mid-plane region, which has the highest heat and particle loads on limiters, i.e. the main chamber samples were from the erosion zone and free from any deposits and impurity co-deposits. After 15 hrs of annealing at 513 K, the remaining D fraction was over 90% [222] indicating the D to be retained in energetically deep and implantation-induced defects in the bulk Be.

### 3.4. Hydrogen isotope exchange experiments in Be co-deposits

Isotope exchange has been proposed as one possible way for intermittent reduction of tritium retention in ITER [221]. Isotope exchange in W, at least in the near-surface region, is very efficient already at low temperatures and low fluences [241,242]. However, hydrogen isotope retention in ITER will be limited by codeposition with Be in thick layers rather than by implantation near the surface. Therefore isotope exchange is not expected to reduce tritium retention for Be substantially. Still, for W it has been proven to be a method to study the dynamics of hydrogen isotope transport in general by switching from one isotope to the other [241,243]. As hydrogen transport in Be is much less understood than in other metals it might therefore be a way to elucidate the mechanism of transport.

To study the isotope exchange effect in Be, a D-containing Be co-deposit grown in PISCES-B up to a thickness of 50 nm was exposed to a low energy 200 eV/D ion beam with a flux of $2 \times 10^{19}$ $Dm^{-2}s^{-1}$ and the exchange of H by D was subsequently measured with ERDA. Exchange within the ion range was very effective and 80% of the initially retained D was removed after a fluence of $1{\times}10^{23}$ $Dm^{-2}$ even at room temperature. Exchange of H by D on a 200 nm thick co-deposit showed that exchange happens only within the ion range at this low temperature. Exchange of H by D at 450 K on magnetron sputtered, hydrogen-containing Be films also showed no indication of D uptake or H removal in depth. Magnetron sputtered, hydrogen-containing Be films with thickness of 600 nm were implanted with 10 keV $D_2^+$ ions and the implanted deuterium amount as well as the distribution of hydrogen were measured with ion beam analysis [244]. Homogeneous removal of hydrogen was found with NRA well beyond the implantation zone even at low temperature although D was not found penetrate deeply.

There were several dedicated large-scale isotope exchange experiments in JET-ILW to determine fuel removal efficiency by either tokamak plasma discharges, glow discharges or ion cyclotron plasma discharges [245,246]. Gas balance analysis of the isotopic ratio carried out at the plasma changeover experiment, from H to D and from D to H, have shown fuel release predominantly from the surface layers of the Be wall and the W divertor [245]. The most promising technique with the highest fuel exchange or removal is the ion cyclotron wall conditioning (ICWC) since there is, in particular, no co-deposition of the released fuel particles as there would in a tokamak discharge. Therefore, it has been concluded that the changeover from D-T to H plasma at the end of a discharge in ITER may only reach the easily accessible short-term fuel reservoir. ICWC aiming at the D inventory reduction by isotope exchange with H has shown positive trend, though better statistics regarding the operation conditions and access to the region of Be co-deposits in the divertor and the limiter plasma-shadowed sides is needed [246]. The impact of the fuel change, from D to H, on the surface hydrogenic composition of PFCs has been studied following the second ILW campaign (ILW-2) which was finished with approximately 300 tokamak plasma shots in hydrogen [191,247]. The content of deuterium in the near-surface layer of the co-deposits measured with NRA was decreased by approximately 30% in comparison to the situation after first campaign (ILW-1) performed fully with deuterium fuelling. The depletion of deuterium content after ILW-2 was also confirmed by secondary ion mass spectrometry (SIMS) [191].

## 4. Spectroscopic data

Optical emission spectroscopy (OES) provides in situ access to gross erosion rates, impurity concentrations and fuel content during plasma operation. The Be source strength resulting from physical sputtering is usually addressed by observation of the neutral (Be I) or single ionized Be (Be II). Doubly ionized Be (Be III) in the SOL region can either describe energetic impinging Be impurities or transported and further ionized Be from the source. Conversion of the light emission is done with the aid of photon emission coefficients, which are tabulated e.g. in the Atomic Data and Analysis Structure (ADAS) database.

### 4.1. Beryllium spectroscopy simulations - ADAS

The international project ADAS is a software package which provides computational plasma modelling tools and databases for analysis and interpretation of spectral measurements for fusion and astrophysical applications [248].

The choice and correct use of Be atomic data, including the effect of quasi-metastable (qMS) levels (the ground state $1s^2 2s^2\ (^1S_0)$, and the metastable $1s^2 2s^2 p\ (^3P_0)$) is of importance for correct Be spectroscopy simulation. The ERO code, which is used for simulating various PSI events and solves the 3D kinetic equations of impurities migrating in the edge plasma [212,249], has been used for modelling by including ADAS data, which is one of the most systematic and up-to-date compilations of the ab-initio calculated data of rates for fusion-relevant collisional processes. The data is organized in a flexible collisional-radiative model (CRM) allowing various level reductions of itself to

the effective rates, which can be deployed further in plasma transport codes, such as ERO.

ADAS contains multiple datasets for each element and its ionization states (i) the standard unresolved, JET baseline data with low precision, but which is fairly complete (labelled as ADAS'89); (ii) the metastable-resolved data set, but which is available only for light elements with primary relevance to fusion (labelled ADAS'93), and (iii) the high-grade metastable-resolved data set (labelled ADAS'96). For instance, for Be I the data sets ADAS'93 and ADAS'96 are widely used, however, at low energies the ionization data in set ADAS'93 is known to be, on average, a factor two too low [250]. The data set ADAS'96 has more levels and transitions included, and it provides intermediate coupling for all Be ionic states as well as the qMS levels for Be I and Be II. The inclusion of qMS levels allows the relatively slow relaxation between two spin systems, such as the triplet and singlet for Be I with two upper shell electrons, to be followed without the need of full-size CRM calculations if the respective effective rates are used. For instance, for line emission intensities there are as many photon efficiency coefficients (PEC) as the number of qMS traced. Still, if this precision is not needed a single PEC, or e.g. an ionization rate based on the very same dataset assuming that qMS are in Boltzmann equilibrium can be produced. Exporting the reduced atomic and ionic data from ADAS to the plasma particle tracing codes is computationally efficient, but further dataset development may be needed in the future.

The computational price when applying MS-resolved data is tracing the level population ($\chi$) and having significantly more rates. However, the number of rates is still much less than in full-size CRM. In addition, when using MS-resolved data for Be an arbitrary initial qMS level population just after a Be sputtering event from the PFCs can be assumed. Recent analyses have shown that assuming an $\chi = 0.66 - 0.75$ population ratio in Be I corresponding to the $1s^2 2s^2 p\ ^3P_0$ level with the ground state leads to best agreement with the experimental PWI results obtained in PISCES-B and JET-ILW with D, He and Ar plasmas [251]. The origin for this specific population level has remained unclear and more research is required in solid state and atomic physics. In some cases the sputtered Be I species get ionized or thermalized with the surrounding plasma relatively soon after the PWI event, so that this initial population has no effect on the measured spectroscopic results. Moreover, the difference in ionization from the ground state ($1s^2 2s^2$) and the metastable ($1s^2 2s^2 p$) is ≈20–25%, so these processes can often also be neglected. However, for line intensities of neutral lines near the erosion or sputtering location, the effect is critical and cannot be neglected. The effect has been seen to vary by a factor of three or more between population levels $\chi = 0$ and $\chi = 0.75$. Obviously, the effect is the opposite for singlet and triplet lines for Be I decaying from respective qMS levels. Thus, it is of great use to have a measurement of line ratios, which allow the determination the initial $\chi$ just after Be sputtering. For the highest precision the measured singlet and triplet line intensities should be used, which is, unfortunately, not always easy given that the strongest singlet lines, including the resonance line (Be I at 234.9 nm), lie in the UV range. In experiments at PISCES-B it has been shown that the Be I 373.7 nm line can also be deployed successfully for this purpose [252].

### 4.2. Experimental data

A spectroscopic method is widely used to quantify the sputtered atomic Be flux [253,254]. In this method, the line intensity can be converted to the sputtered flux with a spectroscopic parameter, so called $S/XB$, as follows. The sputtered flux of Be atoms, $\Gamma_{\mathrm{Be}}^{\mathrm{Spt}}$, is expressed as,

$$\Gamma_{\mathrm{Be}}^{\mathrm{Spt}} = \Gamma_{\mathrm{Be}\rightarrow\mathrm{Be}^+} + \Gamma_{\mathrm{Be}}^{\mathrm{GL}}, \tag{1}$$

where $\Gamma_{\mathrm{Be}\rightarrow\mathrm{Be}^+}$ is the ionization flux of Be atoms, and $\Gamma_{\mathrm{Be}}^{\mathrm{GL}}$ is the geometrical loss flux of Be atoms. When $\Gamma_{\mathrm{Be}}^{\mathrm{GL}}$ is negligibly small, which is the critical condition of the method, Eq. (1) can be written as,

$$\Gamma_{\mathrm{Be}}^{\mathrm{Spt}} \approx \Gamma_{\mathrm{Be}\rightarrow\mathrm{Be}^+} = 4\pi \frac{S}{XB} I_{\mathrm{Be}}. \tag{2}$$

Here, $I_{\mathrm{Be}}$ is the Be I line intensity. Thus, $S/XB$ is an essential parameter to quantify the sputtered flux. For Be I, $S/XB$ values of the strongest visible line at 457.3 nm were experimentally determined under He plasma exposure to a Be target in PISCES-B [255]. From Eq. (2), $S/XB$ can be obtained as,

$$\frac{S}{XB} \approx \frac{\Gamma_{\mathrm{Be}}^{\mathrm{Spt}}}{4\pi I_{\mathrm{Be(I)}}} = \frac{Y_{\mathrm{Be}}\Gamma_{\mathrm{i}}}{4\pi I_{\mathrm{Be}}}, \tag{3}$$

if $\Gamma_{\mathrm{Be}}^{\mathrm{Spt}}$ is known. The incident ion flux, $\Gamma_{\mathrm{i}}$, was measured with a Langmuir probe. The sputtering yield of Be by He bombardment, $Y_{\mathrm{Be}}$, was determined to be $\sim (2\pm0.4)\times10^{-3}$ at the incident ion energy, $E_{\mathrm{i}}$, of ~ 35 eV from a mass loss measurement in a dedicated plasma exposure at low $\Gamma_{\mathrm{i}}$ to avoid the redeposition of sputtered Be atoms on the target.

To satisfy the critical condition that $\Gamma_{\mathrm{Be}}^{\mathrm{GL}}$ is negligible (in other words, most of sputtered Be atoms need to be ionized before escaping from the plasma column), the measurements of $I_{\mathrm{Be(I)}}$ were carried out at higher $\Gamma_{\mathrm{i}}$ for pulsed plasma discharges of several tens of seconds to avoid the overheating of the Be target. When the ionization mean free path, $\lambda_{\mathrm{mfp}}$, of sputtered Be atoms was measured to be around 6–9 mm, the fraction of geometrical loss flux of sputtered Be atoms, $\Gamma_{\mathrm{Be}}^{\mathrm{GL}}/\Gamma_{\mathrm{Be}}^{\mathrm{Spt}}$, was estimated to be ~8–18%. Here, $\Gamma_{\mathrm{Be}}^{\mathrm{GL}}/\Gamma_{\mathrm{Be}}^{\mathrm{Spt}}$ was calculated from $\exp(-L/\lambda_{\mathrm{mfp}})$ with the characteristic length of the system $L$ = 15 mm taken from the plateau radius of the plasma parameters. Thus, $S/XB$ may be overestimated by <50% [256] because of the underestimated $I_{\mathrm{Be(I)}}$. However, measured $S/XB$ values were ~3–5 times lower than calculated data from ADAS'96 [248].

From the results obtained with PISCES-B some interpretations can be derived. The systematically lower measured $S/XB$ values as compared to ADAS values may be ascribed to the underestimation of $Y_{\mathrm{Be}}$. In the estimation of $S/XB$, $Y_{\mathrm{Be}} \sim (2 \pm 0.4) \times 10^{-3}$ from the mass loss measurement was used as mentioned above, which is ~ 10 times lower than the TRIM value [257]. The lower $Y_{\mathrm{Be}}$ can be explained mainly by surface morphology development [258] during the mass loss measurement. On the other hand, surface morphology was not fully developed for the $S/XB$ measurements because of the pulsed plasma discharges, i.e. low incident ion fluence to the target. The actual $Y_{\mathrm{Be}}$ during the $S/XB$ measurements is, therefore, speculated to be somewhat higher than $Y_{\mathrm{Be}} \sim (2 \pm 0.4) \times 10^{-3}$, leading to an increase in $S/XB$ and to better agreement with ADAS. However, more research is needed to properly explain the differences in experimental and ADAS data.

## 5. Beryllium erosion, deposition and hydrogen retention at JET

### 5.1. Measurements

The operation of JET started in 1983 as an all-metal machine. In 1984 carbon wall components were introduced on the inner wall cladding and limiters, thus starting the operation of JET-C (1984–2009). Application of Be for wall conditioning began in 1989 through Be evaporation (performed regularly until 2009) and the use of bulk Be for major PFCs: (a) belt limiter composed of over 2000 castellated tiles and for the floor tiles covering the Mk-0 divertor operated for about 56 000 secs in 1989–1992, and (b) castellated tiles of the Mk-I-Be divertor operated in 1995. Details of the operation and of consecutive divertors are presented in Ref. [146]. The size of the device (being still the largest tokamak in the world) and the recently installed [259,260] ITER-Like Wall (JET-ILW) with Be on the main chamber wall and W in the divertor provide erosion and retention data at the most relevant conditions for ITER.

All measurements at JET [262] should be separated in two large groups: in situ and ex situ measurements. The latter comprises post-campaign, or *post-mortem* analysis of the PFCs after they are retrieved from the machine. The crucial difference lies in the way in which both types of data can be interpreted. The practice of tokamak operations is

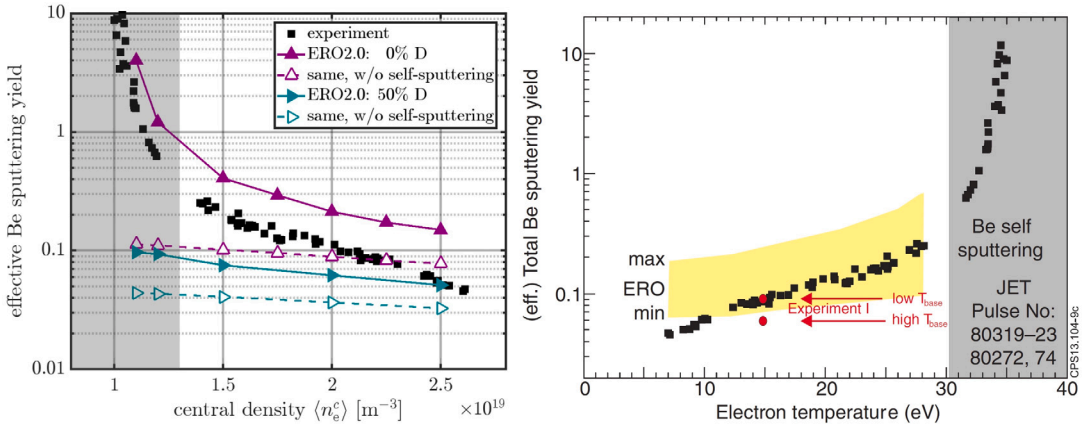


**Fig. 4.** Comparison of computational ERO2.0 and experimentally measured effective Be sputtering results with JET-ILW limiter plasma conditions as a function of electron density, $n_e$ (left), and temperature (right). Also shown is the computated Be sputtering result using Be target with 50% D ("ERO-min") and pure Be target ("ERO-max") approximations (yellow shadowed area). (For interpretation of the references to colour in this figure legend, the reader is referred to the web version of this article.)
*Source:* Reproduced from Refs. [164,261].

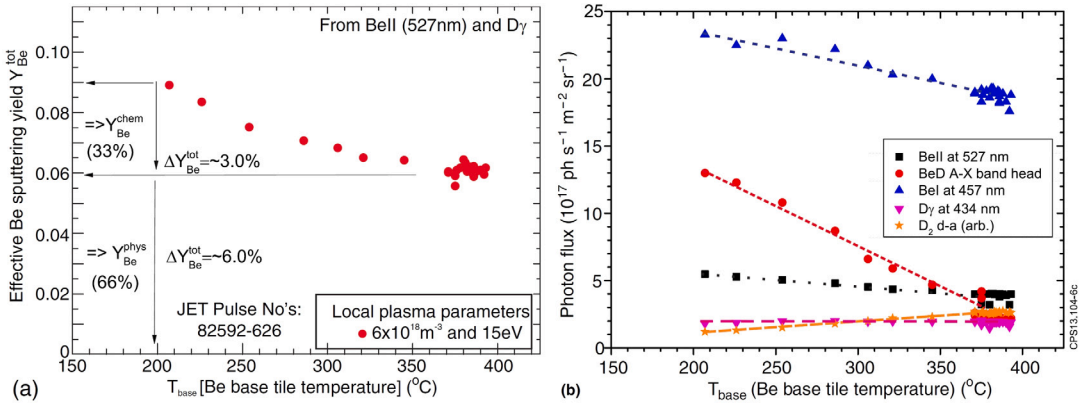


**Fig. 5.** Temperature dependence of the experimentally measured effective Be sputtering in JET with ILW. Left: Chemical ($Y^{chem}$) and physical ($Y^{phys}$) sputtering yield of Be. Right: Spectroscopic data for Be and D atomic species and for BeD and $D_2$ molecules.
*Source:* Reproduced from Ref. [261]

that the sample extraction can in most cases be done only during the shutdown phases, which take place after long experimental campaigns. In total the wall is exposed to a large number of plasma discharges with various configurations (e.g. safety factor $q$, heating power, wall clearance, strike point position, seeding of various plasma diagnostic and control gases), and therefore different plasma parameters and PWI conditions. All these make it virtually impossible to obtain the exact conditions determining the PWI experienced by an individual PFC during a campaign hence making post-mortem data interpretation highly demanding. Further, plasma conditions always vary, even across a single wall element during a pulse. Some tokamaks are equipped with manipulators or shutters allowing sample exposure for a dedicated period and its removal and exchange without the need for the vent of the tokamak vessel. However, such setup is not available at JET.

### 5.1.1. *In situ measurements*

This section focuses on the in situ measurements at JET, which are mostly spectroscopic, because they can be interpreted by a direct modelling of any instant plasma conditions and configuration as described below. JET is equipped with a number of spectroscopic sightlines measuring integrated light in various spectroscopic ranges. Some of these look in the horizontal direction (coming normal or tangential to the inner wall elements) at the midplane; others look into the JET-ILW divertor from the top of the machine. Multiple sightlines provide certain spatial resolution. The light is often split and registered by various spectrometers and photomultiplier tubes providing various optimizations for time and spectral resolution.

A combination of optical emission spectroscopy (OES) and limiter discharges have been applied at JET to measure in situ the gross erosion of Be under controlled plasma conditions. Limiter discharges with different fuelling rates were used to provide a variation of local plasma conditions and the incident energy of impinging ions. Fig. 4 shows the variation of the effective Be sputtering yield, determined by $S/XB$ method, as a function of the plasma density and electron temperature (described in Ref. [261] and Section 4.2). The effective Be sputtering yield is the total sputtering composing of Be physical sputtering and CAPS (Section 3.2.2). The presented "ERO-max" calculation assumes sputtering from a pure Be lattice, whereas the "ERO-min" calculated value assumes Be sputtering from a surface containing 50% D within the Be lattice. At low electron temperatures the sputtering is caused by deuterons, whereas at higher temperatures (> 30 eV), self-sputtering by Be ions becomes dominant. ERO2.0 has been successfully used in modelling these experimental results [164].

The limiter discharges lead also to the increase of the surface temperature of the Be limiters, which in turn leads to a change of the local sputtering mechanism of Be. It was found that the CAPS mechanism is a relevant release path in the case of JET at low Be surface temperatures.

Up to 1/3 of the gross erosion could be attributed to the CAPS release mechanism as shown in Fig. 5 which was deduced from OES on the BeD A-X band emission and Be I and Be II line emission [261]. The CAPS mechanism is linked with the D concentration in the near-surface

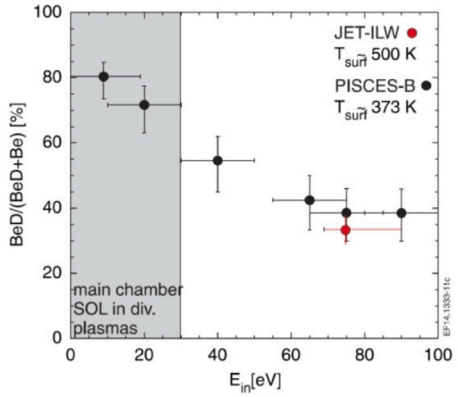


**Fig. 6.** Experimentally measured release of BeD from Be surfaces as function of impact energy in the JET-ILW and compared with PISCES-B data.
*Source:* Reproduced from Ref. [148].

region. Without sufficient deuterium reservoir present, the release of chemical compounds by physical impact is much reduced, and therefore at higher surface temperatures and lower fuel content in the Be surface, less molecular-related sputtering can be expected and physical sputtering will be dominant. In addition to surface temperature, the energy of impacting D ion has a decreasing effect to the formation of sputtered BeD molecules (Fig. 6). These analyses are specific only for well-defined limiter conditions with plasma contact and which are described in detail in Ref. [261]. The observations are in-line with MD calculations (Ref. [218] and Section 6.2) and with linear plasma studies in PISCES-B [263].

The situation is more complex in the case of diverted plasmas when the separatrix is between 5 and 10 cm away from the first wall. In these plasma discharges, residual ion flux to the wall and CX neutrals determine the global source of Be. Deconvolution can only be done with the aid of modelling as CX neutral fluxes are not directly measured; both WallDYN and ERO2.0 codes, applied with an appropriate plasma background have been used. Fig. 7 shows a comparison of experimental data from OES during JET reference pulses in limiter, ohmic, L- and H-mode conditions and the corresponding ERO2.0 modelling results. The experimental and the ERO2.0 modelling results are in good agreement in the limiter phase and in fair agreement in the H-mode phase, which is mainly caused by the uncertainties in extrapolation of plasma conditions to the first wall. Also shown in Fig. 7 is the complete 3D analysis of Be gross erosion and Be net deposition in JET-ILW. This methodology has allowed benchmarking of the code, which has been qualified for predictions for different ITER plasma conditions [161].

### 5.1.2. Ex situ measurements

Despite the complexity of post-mortem data interpretation described above, a number of valuable results were obtained, giving insight on the general distribution of erosion, deposition and fuel retention [191] along the Be–W wall [247] or, for instance, the impact of Be castellation (gaps) on the PSI issues [264]. In addition, as mentioned in Section 3.3.2, ex situ analyses have allowed for validation of global migration codes such as WallDYN. The experimental methodologies applied in the retention and co-deposition analyses have been listed in Section 3.1.

The gradual introduction of Be in JET since 1989 [265] allowed for studies of material-dependent fuel retention and material migration. Fig. 8(a) shows the JET-C vessel wall with Be tiles on the floor and in two toroidal belts of limiters comprising in total about 2000 castellated blocks, which are shown in detail in Fig. 8(b): 36 cm long and 16 mm wide, castellated every 16 mm with a 1 mm wide groove. Details of the exposed tiles are on the accompanying images: exposed surfaces with molten and unaffected areas (Fig. 8(c)), side surfaces located in the gap between the tiles showing the extent of deposition (around 16 mm deep into the gap) and also demonstrating that the castellation grooves are free both from dust and molten metal even in the areas of melting on PFS (Figs. 8(d)–(e)); view of two surfaces inside the castellation gap showing shallow deposition, only 2–3 mm deep into that narrow gap (Figs. 8(f)–(g)). Analyses performed after ≃56 000 s of plasma operation have shown that: (i) deuterium retention was associated with co-deposition of carbon eroded from the inner wall cladding and upper limiter tiles, and (ii) the deposition increases with the gap width [266].

In 1994 the Mk-I divertor was implemented. First it was operated with tiles made of carbon fibre composites (Mk-I-CFC) and in 1995 with Be tiles (Mk-I-Be). Operation with Mk-I-Be was for 20 303 s including of 9153 s of diverted plasma. The divertor was composed of roof-shaped, castellated Be blocks 72 mm long poloidally, 30–40 mm wide toroidally, 50 mm high, separated by gaps either 6 or 10 mm wide and castellated 6 x 6 mm with a 6 mm deep and 0.6 mm wide groove. A general view of JET-C with the Mk-I-Be divertor and details of the tiles are shown in Figs. 9(a)–(d). Deuterium on these tiles has always been detected together with carbon originating from the erosion of the main chamber limiters, thus indicating that co-deposition occurs in the gaps between tiles and to some extent in the grooves of castellation but only 1–2 mm deep into the groove, as shown in Fig. 9(e) [267]. No D was detected to be retained in bulk Be. The retention in the Be tiles was much smaller than on the previously operated Mk-I-CFC components [177,268]. As stated above, all C found in the Be divertor must have originated from erosion of the main chamber wall, so that the differences between the CFC and Be divertors may be attributed to the lack of the local C source in case of the Be divertor floor.

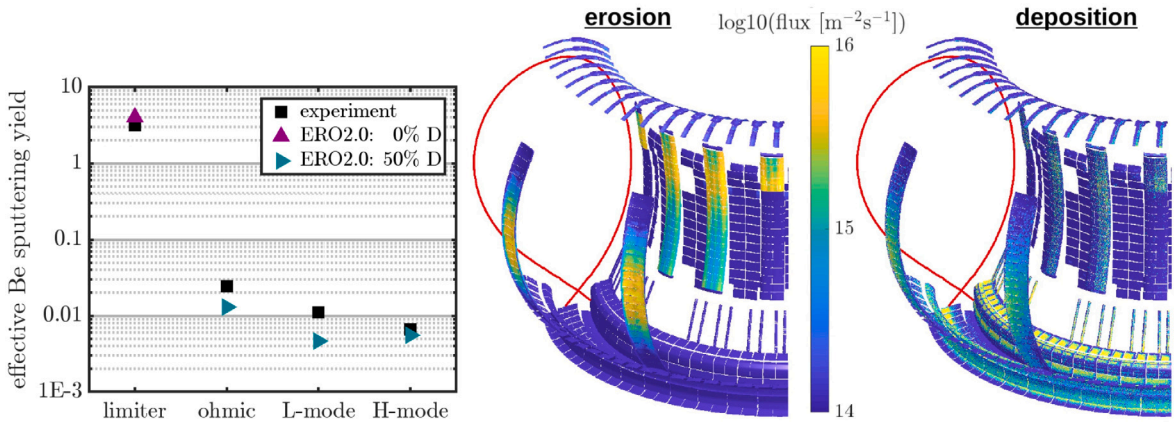


**Fig. 7.** Comparison of experimental spectroscopy and ERO2.0 modelling on effective Be sputtering in different JET-ILW plasma scenarios. Also shown the main Be erosion and deposition zones in JET-ILW as obtained with ERO2.0.
*Source:* Reproduced from Ref. [164].

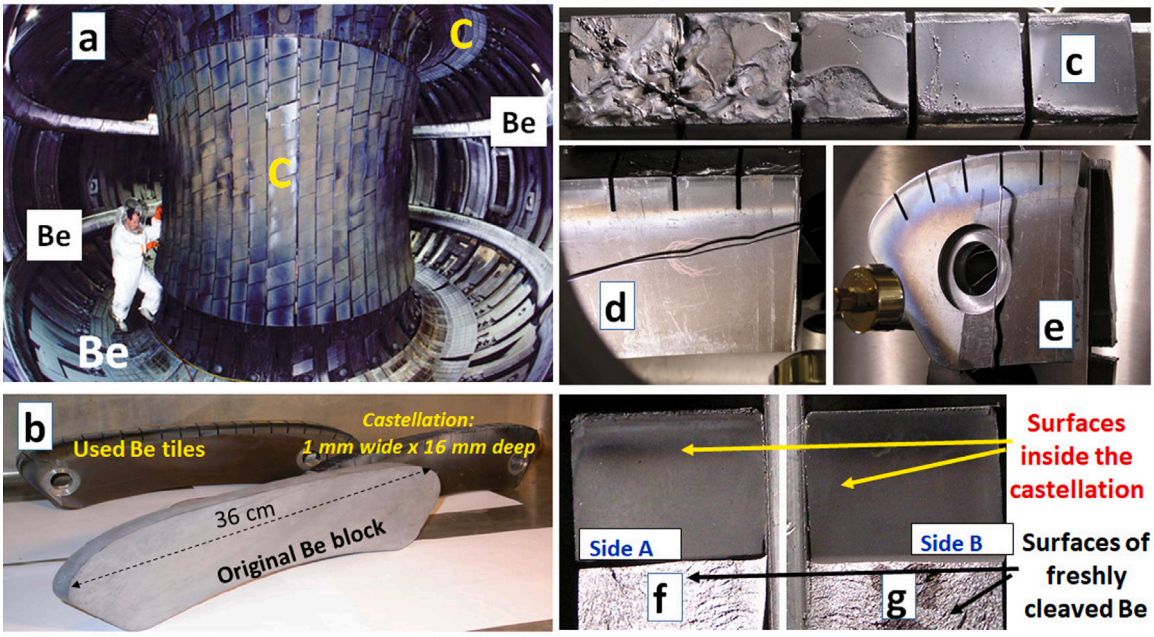


**Fig. 8.** View inside the JET vessel with Be components: (a) floor of the Mk-0 divertor and belt limiters, (b) Be tiles of the belt limiter, (c) surface topography of plasma-facing surfaces, (d) and (e) side surfaces of limiters, (f) and (g) cleaved limiter with surfaces inside the groove of castellation and those freshly opened by cleaving.

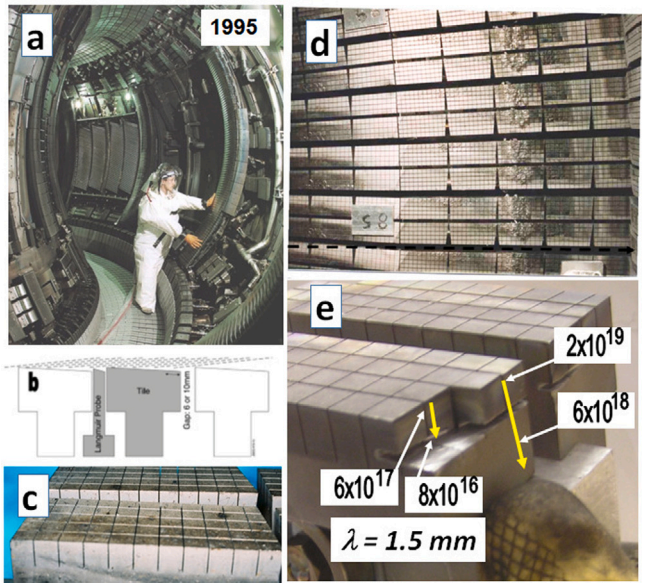


**Fig. 9.** (a) View inside of JET with the castellated Be limiter tiles of the Mk-I(Be) divertor operated in 1995. (b) A schematic view showing the arrangement of the Be divertor tiles and the location of Langmuir probes. (c) Side view of castellated Be divertor tiles showing the castellation gaps being clean of molten material and dust. (d) Top view of the inner and outer divertor showing melt zones. (e) D distribution on side surfaces between the tiles and inside the castellation.

Images in Figs. 10(a) and (b) show respectively the all-metal JET-ILW vessel and the tile map with the colour-coded distribution of the wall materials. All Be tiles are castellated to ensure thermo-mechanical durability and integrity of materials under high heat flux loads: 12 × 12 mm net with a 12 mm deep and 0.4 mm wide groove. In total there are 1183 tiles with 168 203 castellated blocks [264] with a total weight exceeding 2.5 tonnes. In addition, inner wall cladding (IWC) tiles are coated with evaporated 8 μm-thick evaporated films; around 12 kg of Be [269,270]. Detailed views of the different limiter types are shown in Figs. 11(a)–(f).

To enable material migration and fuel retention studies, a set of erosion–deposition diagnostic tools has been installed in the divertor and on the main chamber wall: marker tiles and a package of wall probes described in detail in Ref. [271]. For ex situ examinations they have been retrieved and exchanged by new sets during major shut-downs after consecutive campaigns in 2011–2012 (ILW-1), 2013–2014 (ILW-2) and 2015–2016 (ILW-3). In addition, dust has been collected (for details see Section 5.3).

An overview of Be migration mechanisms in JET-ILW is given in Ref. [64]. The general migration paths for limited and diverted plasma configurations are depicted in Fig. 12. Be is eroded from limiters in the main chamber by ions and CX neutrals from the plasma. A detailed quantitative description based on profiling tiles from the inner and outer wall limiters has been given in Ref. [272], while massive erosion and material splashing from the upper dump plates (UDP) is discussed in Ref. [169]. The eroded and ionized material migrates along the SOL magnetic field lines and is transported to the divertor. The poloidal cross section of the W divertor is shown in Fig. 13, where tile numbers and poloidal S-coordinate are indicated. The main deposition area is in the upper part of the inner divertor where co-deposited Be-rich layers are formed: especially on Tile 0 and on the so-called apron (top flat part) of Tile 1 (S-coordinates 0–227 mm introduced in Fig. 13). The retained fuel, around 0.3% of the injected gas, is detected mainly in layers formed on the upper part of the inner divertor (Table 1). Their thickness reached around 10 μm [262,273–276] as measured after ILW-1, and 20 μm after ILW-2 [191,277]. It should be stressed that Be-based co-deposits are significantly thinner than the C-layers formed on the wall components of JET-C. This is because of the strong reduction of the C source (only residual C in JET-ILW and no chemical erosion of Be), reduced Be transport to the shadowed areas in the divertor (limited long-range transport of Be), and significantly lower fuel retention in the Be-rich co-deposits. JET-ILW divertor deposits consist mainly of Be with 3–20 at.% of C, O, N and small amounts of Ni and W [191,247,275,278].

The retention by implantation and co-deposition on PFSs of Be limiters constitutes around 30% of the total retention on such surfaces (see Table 1 and Ref. [65]). In addition there is transport to the grooves of tile castellations, where the deuterium fuel is deposited at the very entrance of the castellated groove: a shallow deposition pattern

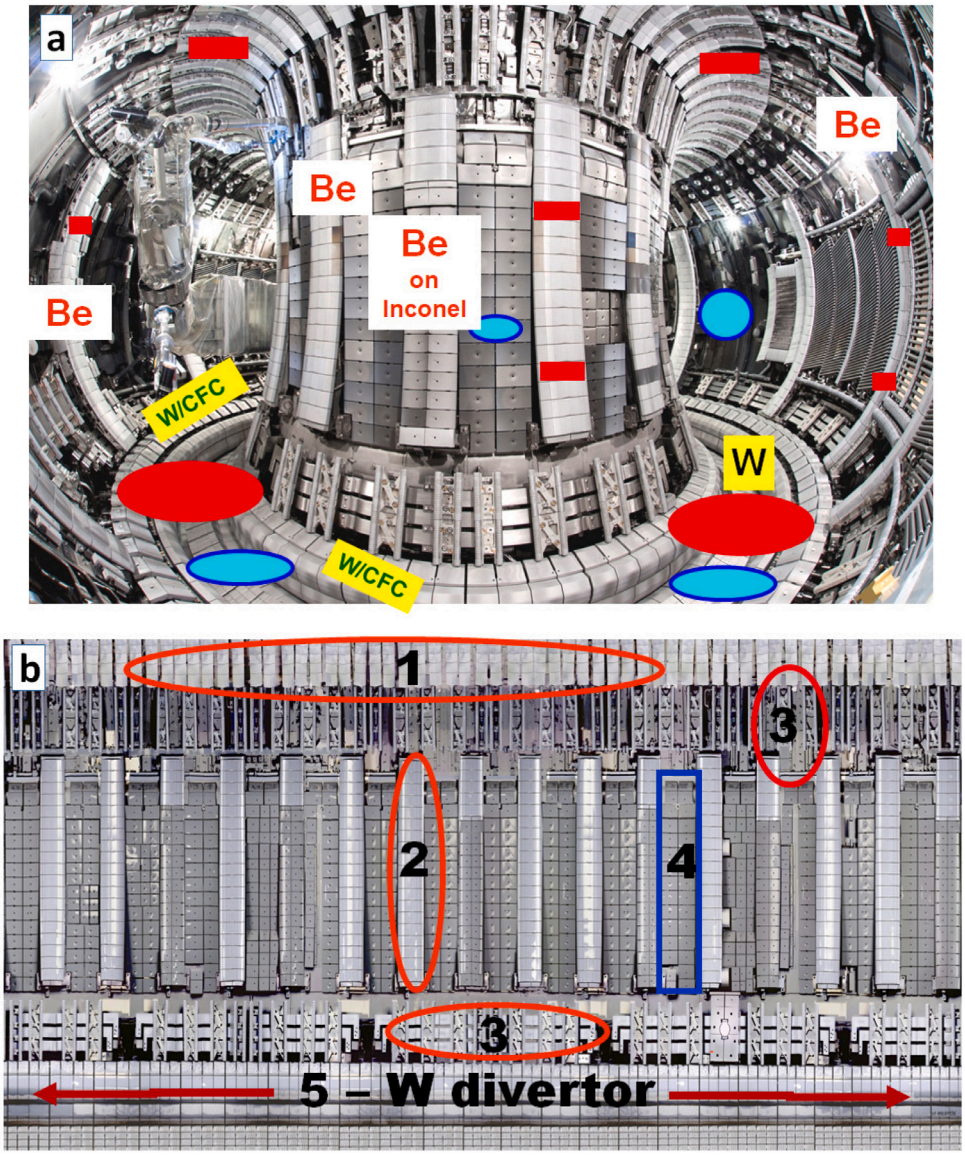


**Fig. 10.** (a) Inside of JET with Be and W PFCs of the ILW. Schematically marked the locations of erosion–deposition diagnostics: marker tiles (red) and wall probes (blue). (b) Map of PFCs on the high field side of JET-ILW: 1-Be upper dump plates, 2-Be inner wall guard limiters, 3-Be coil protection, 4-Be-coated Inconel tiles on the inner wall, 5-components of the W divertor. (For interpretation of the references to colour in this figure legend, the reader is referred to the web version of this article.)

reaching only 0.5–1.5 mm into the 12 mm deep gap and low D content not exceeding $4 \times 10^{18}$ at./cm$^2$ [264]. The modelling has also shown a very significant increase of deposition (and inventory) with the increase of the gap width, e.g. over 10 times when the width of castellation is increased from 0.5 mm to 2 mm.

Analysis of PFSs of Be limiters with X-ray diffraction (XRD) has clearly shown two distinct composition patterns: Be–W mixed intermetallic compounds on the sides of limiters (deposition zone), whilst only pure Be is detected in the erosion zone [264]. The formation of thin layers containing Be–W intermetallic compounds on the inner divertor vertical tile has also been identified using XPS [234,280].

Unlike the bulk Be limiters, the recessed Be-coated IWC tiles are not affected directly by the plasma: (a) no significant deviation from the original coating thickness has been detected, (b) the surface content of deuterium is in the range $(0.9–1.7) \times 10^{17}$ cm$^{-2}$, and (c) the bulk content of deuterium in Be does not exceed 0.2 at.%, and most likely comes from CX neutral implantations. The fuel level indicates that a single IWC tile does not constitute a major trapping site for hydrogen isotopes. However, due to the large total surface area formed by all the

**Table 1**
Summary of the retained D total amounts in JET-ILW in-vessel components as measured after ILW-1 campaign [191].

| JET vessel component | Number of D atoms |
|---|---|
| Upper dump plates[a] | $2.1 \times 10^{22}$ |
| Outer poloidal limiters[a] | $5.2 \times 10^{22}$ |
| –outer wall[d] | $8.8 \times 10^{21}$ |
| Inner wall guard limiters[a] | $1.4 \times 10^{22}$ |
| –recessed limiters[c] | $1.1 \times 10^{22}$ |
| –inner wall (IWC tiles)[b] | $1.7 \times 10^{22}$ |
| Divertor (excl. tile 5[e]) | $2.1 \times 10^{23}$ |
| –inner divertor[c] | $1.7 \times 10^{23}$ |
| –outer divertor[c] | $3.9 \times 10^{22}$ |

[a]Bulk Be tile.
[b]Be-coated tile.
[c]W-coated CFC tile.
[d]W-coated CFC tiles and steel surfaces.
[e]Bulk W tile.

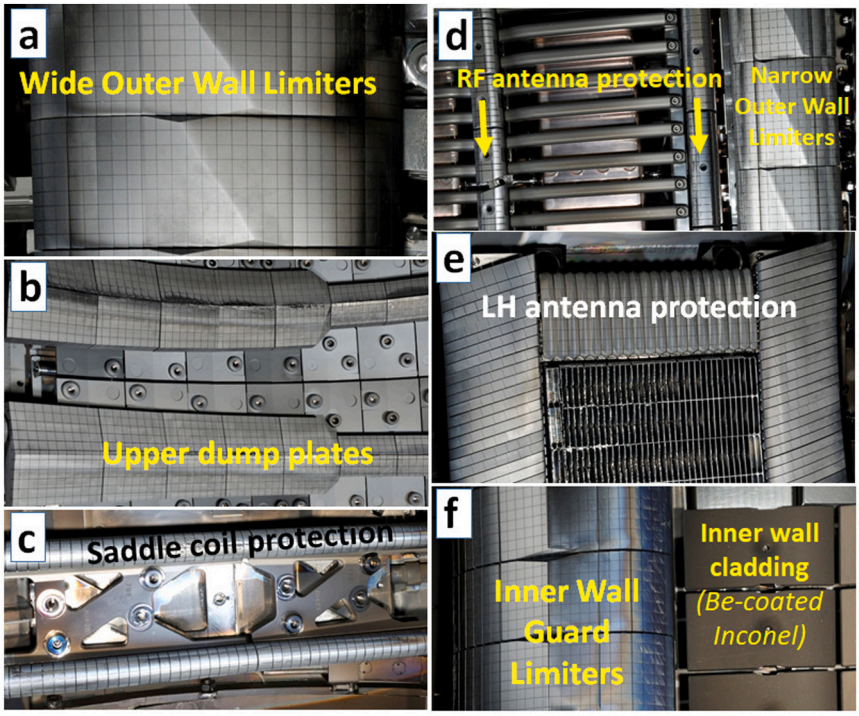


**Fig. 11.** Details of Be components of JET-ILW: (a) outer wide poloidal limiters, (b) upper dump plates, (c) coil protection tiles, (d) RF antenna protection tiles and outer narrow poloidal limiters, (e) lower hybrid antenna protection tiles, (f) inner wall guard limiters and Be-coated Inconel tiles of the inner wall.

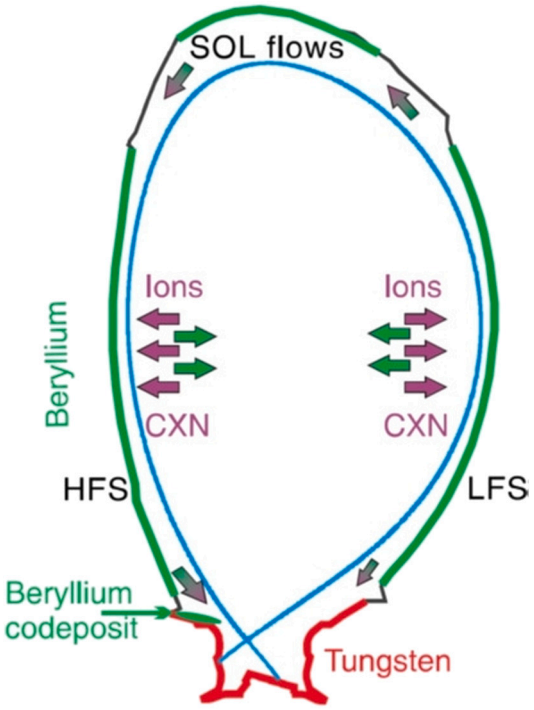


**Fig. 12.** Be migration paths in JET-ILW. Main chamber components in the plasma high- and low-field side (HFS and LFS) interact with ions and CX neutrals from the plasma. Eroded Be particles flow in the SOL ending up deposited mainly in the inner divertor.
*Source:* Reproduced from Ref. [148].

IWC tiles, the global amount of the retained fuel is found to be as high as on the inner wall limiters (see Table 1).

Be and other species are transported to the remote areas of the divertor (i.e. areas shadowed from the direct plasma line-of-sight)

**Table 2**
Total amounts of D, Be and C impurities deposited in the JET-ILW divertor during three operational campaigns [279].

| Impurity | ILW-1 | ILW-2 | ILW-3 |
|---|---|---|---|
| D | 0.9 g | 0.7 g | 0.9 g |
| Be | 53 g | 60 g | 46 g |
| C | 13 g | 7 g | 6 g |

principally when the plasma strike points are on the corner tiles: Tile 4 in the inner and Tile 6 in the outer divertor. The formation of the Be-rich layers has been measured on various wall probes [247,281–284] and modelled [190,285]. The latter indicates that particles reflected from the line-of sight surfaces experience multiple reflection/scattering events resulting in deposition over all surfaces in the shadowed region. However, a crucial outcome in JET-ILW is the reduction of deposition by factor 30–40 when compared to the deposition in JET-C. As an example, the thickest layers measured on JET-ILW test mirrors, which were found to be 0.8 μm while in JET-C these deposits were thicker than 20 μm [281].

In addition, the ex situ analyses of PFCs retrieved after all the ILW campaigns have consistently shown a significant reduction of the global in-vessel deuterium fuel retention (by a factor of 15–20) in comparison to the previously used all-carbon wall [64,65,146,191]. Further, it has been observed that the D retention in the JET-ILW divertor remained approximately unchanged in all three ILW campaigns [279] and Table 2. This is despite variations in the total and relative co-deposition rates of impurities Be and C in the divertor from campaign to campaign. This makes it challenging to ascertain the pre-dominant D retention mechanism. However, the retained D distribution amounts in the divertor correlate with the Be distribution maximum suggesting a plausible significance of Be-D co-deposition over C–D co-deposition.

### 5.2. Modelling

Erosion of the Be FW, and the physical/chemical sputtering of Be has been further investigated using the 3D local transport and PSI

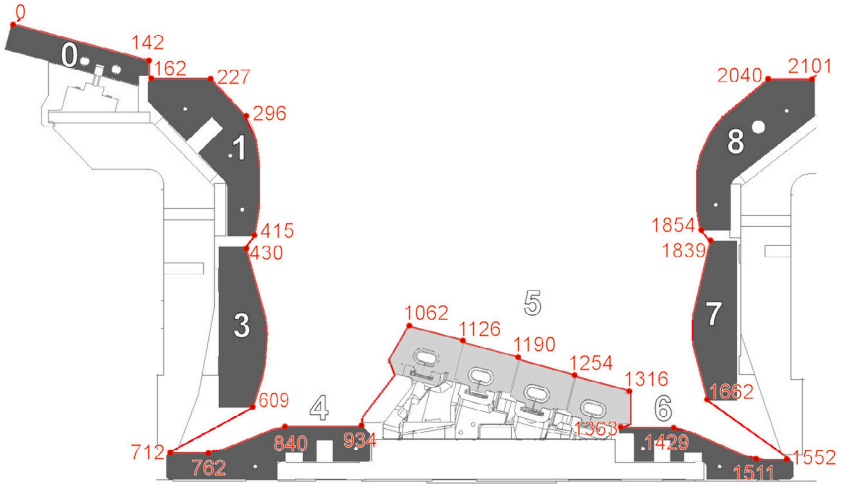


**Fig. 13.** Poloidal cross section of the W divertor of JET-ILW. Tiles are numbered 0–8 and the so-called S-coordinate system (red in mm) defines precisely the poloidal position in the divertor.
*Source:* Reproduced from Ref. [191].

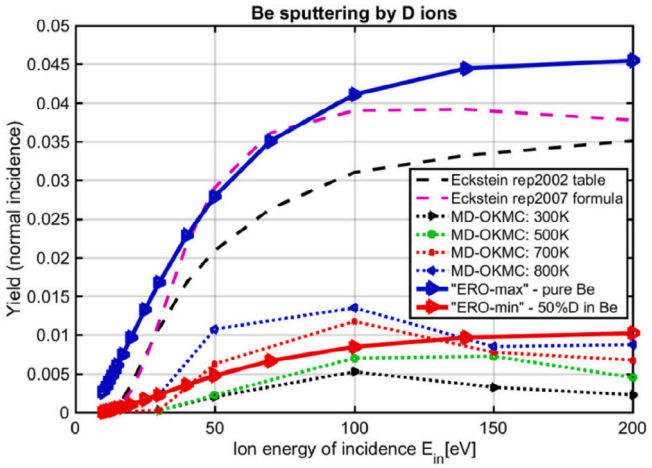


**Fig. 14.** The normal incidence sputtering yields systematically used by ERO for ITER, JET-ILW and PISCES-B simulations: the "ERO-min" and "ERO-max" approximations as well as various BCA results (original 2002 and 2007 data) [289] and MD simulations coupled with OKMC calculations [290].
*Source:* Reproduced from Ref. [291]

Monte-Carlo modelling technique applied in the ERO code [212]. In particular, the OES studies discussed above [148] were interpreted by respective ERO simulations [286]. For the determination of the sputtering Be yields and for the assessment of the erosion data, dedicated experiments were performed with limiter plasmas being shifted towards the inner wall having only a single plasma–wall interaction (PWI) poloidal contact point [261]. It was shown that for the plasma-wetted areas, the best fit of the effective physical sputtering yield (based on molecular dynamic (MD) simulations (Section 6.2.1) and binary-collision approximation (BCA) [287] calculations) was obtained by assuming Be with 50% deuterium in the interaction layer [286]. A procedure for numerical (ERO) or analytic [288] generation of angle and energy distributions of sputtering ions on their impact with surface was suggested and shown to be of importance. Accounting for these effects leads to a unique effective yield for each PFC surface depending on the orientation of the magnetic field with respect to the surface and local plasma parameters.

The sputtering data for Be in the form of fitting parameter set were incorporated into the IAEA database [292]. Data validated with ERO applied to the existing devices was successfully reproduced by the most recent and sophisticated MD simulations [290,291] (see Fig. 14). To reproduce the effect of the D outgassing from the surface, coupling ERO with object kinetic Monte-Carlo (OKMC) simulations was shown to be useful (Section 6.2.1).

In addition, it has been shown experimentally that CAPS contributes up to 50% of all sputtering at surface temperatures of the order of 200 °C, but becomes negligible at higher temperatures (~500 °C) [261]. It is worth mentioning that at the atomistic level the CAPS of Be is a different process compared to the carbon chemical sputtering, and requires a certain threshold energy for the sputtering to take place. The surface, atomic and molecular data were validated by reproducing the experimental Be I, Be II and BeD A-X band spectroscopic emission during the plasma parameter scan.

A crucial influence of the coupled radio frequency (RF) heating power from ICRH antenna on erosion (factor 2–3 increase of erosion yield compared to cases without ICRH) was investigated experimentally by sequential antenna toggling experiments (switching on and off the antennas) and with simulations using the ERO code [293]. The analytical procedure necessary to calculate the local effective sputtering yields was adapted to take into account an additional surface biasing effect due to RF sheath rectification [294]. In the calculations, the same sputtering assumptions were used as for the inner wall simulations (Be target with a 50% D content in the near surface region; labelled as "ERO-min" in Fig. 14) to reproduce the experimental antenna toggling effect. Several key issues need further investigation, such as the fraction of CAPS versus physical sputtering, and the type of $BeD_n$ molecules being released (BeD, $BeD_2$, $BeD_3$). Observations obtained from the JET-ILW, such as the surface temperature and outgassing influence on CAPS, are not yet fully understood nor reproduced in the modelling, and further development is required. One of the main uncertainties for modelling are the plasma parameter backgrounds used, which are remapped in 2D (poloidal cross section) from various diagnostic data sources [289], or simulated using the EDGE2D-EIRENE code [293].

It is important to mention that the same code and sputtering data were also applied to PISCES-B experiments (Section 4.2) where the case of Be sputtering by He was also investigated [252]. Those experiments show that, in this case, the BCA [287] data for pure Be again overestimates the erosion by roughly a factor of 5. Thus, in general the simulations for PISCES-B and JET-ILW are in agreement.

Finally, we conclude for ITER that simulations performed with the validated "ERO-min" model for the erosion yields correspond to the most positive ITER first wall life time ERO predictions [295] (4200 ITER $Q_{DT}$ = 10 discharges, 400 s duration) [158]. It should be mentioned, however, that the "ERO-min" predictions are strongly

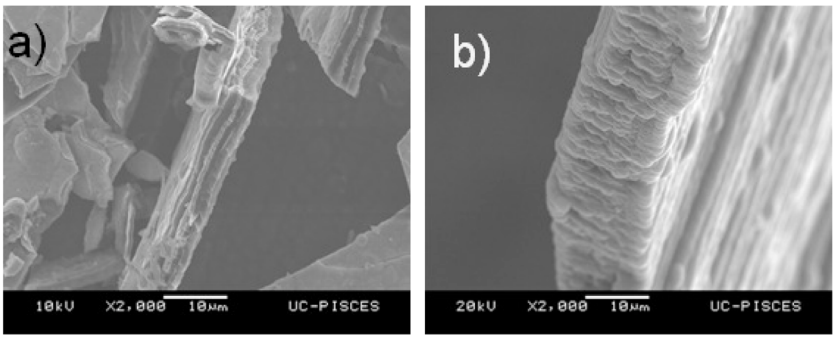


**Fig. 15.** Flakes of dust collected from PISCES-B, (a) newly created flake and (b) an older flake that has been coated with eroded Be.

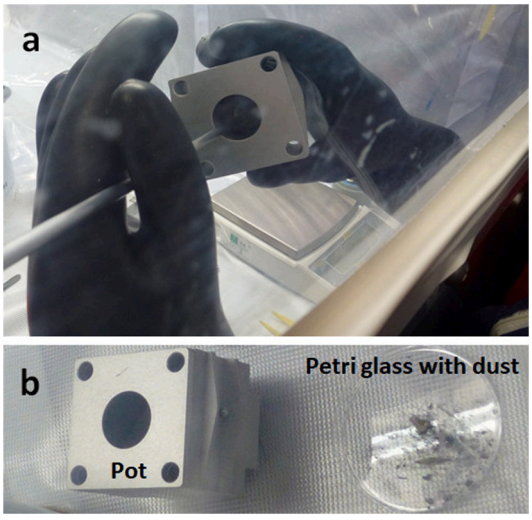


**Fig. 16.** Transfer of vacuum cleaned JET dust from a pot to a Petri glass. Work performed in a glove box at the Be Handling Facility at JET, Culham Science Centre..

dependent on assumptions made on the far SOL plasma in ITER. At this stage, the physics understanding of far-SOL transport in tokamak plasmas does not allow the prediction of the edge plasma properties in ITER. This is a topic of ongoing investigations both experimentally and theoretically. Therefore, the ERO estimates have to be refined using the most recent JET-ILW experience, including the role of CAPS and detailed plasma-shadowing [291] through the improved procedure for the local effective yields (the analytic sheath model mentioned above).

### *5.3. Dust: Results from PISCES-B and JET*

In early experiments with small-scale use of Be-based PFCs (UNITOR [296] and ISX-B [144,145]), no results on dust generation were reported. On a large scale Be has been used only in PISCES-B and JET. In an early study of Be dust in PISCES-B [297], only 40% of the eroded material from prior campaigns could be accounted for; 80% of the measured Be was found in well-adhered coatings within the vacuum vessel. However, it was noted that these coatings were exfoliating and possibly the source of the collected dust. The size distribution of collected dust was also determined, showing an increasing amount of smaller sized particles. Later collection of dust from PISCES-B was not quantified, but showed a larger amount of flaking of the wall coatings [298]. Images from the later dust collection showed that newly formed flakes of dust typically consist of columnar layers of deposits, whereas older Be flakes were observed to have undergone additional Be layer deposition while located within the plasma exposure region of the device, as shown in Fig. 15.

Studies of dust in JET-C started in 1998 after the full D-T campaign. Over 150 g of C-rich co-deposits were found in the divertor in areas shadowed from the plasma line-of-sight [299]. The Be content in that dust was up to 2.4 wt% [146] but no microscopy studies were carried out at that time because of technical issues in handling materials highly contaminated with tritium.

Study of dust from the JET-ILW experiments has been carried out also in response to the ITER needs related to the nuclear safety assessment. A comprehensive research program comprising several dust collection methods: (i) remotely controlled vacuum cleaning of the divertor; (ii) local sampling of loosely bound matter from PFC surfaces using adhesive carbon stickers; (iii) collection of mobilized particles on surfaces of various erosion–deposition probes (EDP) [271] located in the divertor and in the main chamber: dust monitors (Si plates), test mirrors, spatial blocks and covers of quartz microbalance (QMB) devices. A critical assessment of the collection methods has been made in Ref. [300].

Detailed studies require a broad range of techniques and a network of specialized laboratories with ability and expertise in analysis of a broad spectrum of species, from hydrogen isotopes to tungsten and handling of tritium- and Be-contaminated materials. Analyses were performed by a range of methods including scanning electron microscopy (SEM), transmission electron microscopy (TEM) and its scanning variant (STEM), focused ion beam (FIB) [264,281,300–305], energy dispersive X-ray spectroscopy (EDX), electron probe micro-analysis, (EPMA), X-ray photoelectron spectroscopy (XPS) [234,280], standard and microbeam NRA and PIXE [281,300,302,304–306], ERDA [281,300], radiography [307], liquid scintillography (LSC) [308], TDS [300,308,309], total combustion [308] and other techniques. It should be stressed that the X-ray based detection of Be requires both proper detectors and an experienced SEM/EDX operator because of a very low energy of X-ray radiation ($K_\alpha$(Be) = 108 eV). The signal is therefore strongly attenuated even by a thin layer of deposit on Be particles.

The main finding is that the total amount of dust collected by vacuum cleaning after each of the three sequential JET-ILW campaigns is only about 0.9–1.4 g per campaign (with 19.1–23.5 h plasma operation per campaign). This result is obtained despite the fact that the total energy input was increasing in the course of campaigns: 150 GJ, 201 GJ and 245 GJ, respectively, in ILW-1 (2011–2012); ILW-2 (2013–2014); ILW-3 (2015–2016) [191,300,309]. The amount of JET-ILW dust is therefore over 100 times smaller than the collected dust amounts in JET-C [146]. Main reasons for this observed discrepancy can be summarized as (i) there is no chemical erosion of the Be PFCs, (ii) the long-range transport mechanism of eroded particles is lacking in Be wall and (iii) Be deposits are formed as thin layers, which do not show strong flaking, peeling or exfoliation properties. Photographs in Fig. 16 show the transfer of Be- and T-contaminated dust from the pot of the cyclone-type vacuum cleaner to a Petri dish. All operations have been carried out in a glove box of the Beryllium Handling Facility at JET [151] in order to enable preparation of samples for further shipment and studies in qualified external laboratories. Microscopy,

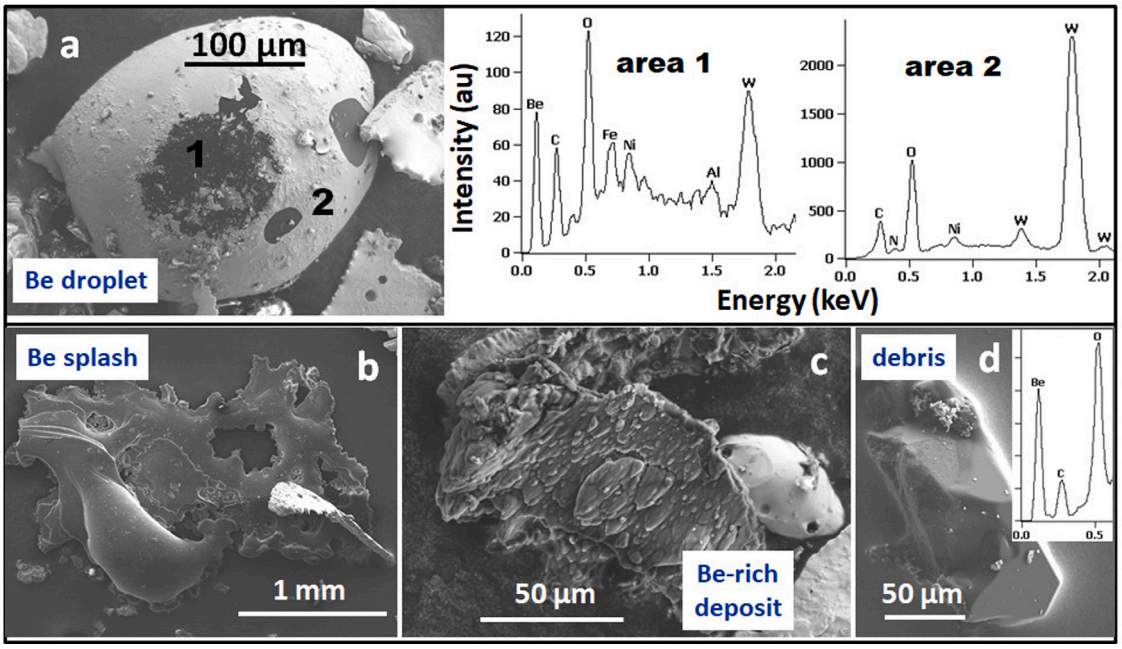


**Fig. 17.** Examples of four categories of Be particles in matter retrieved by vacuum cleaning from the JET divertor after ILW-2: (a) droplet coated with tungsten-rich deposit, (b) splash, (c) co-deposit, and (d) debris from a limiter tile.

EDX and EPMA of the vacuumed grains show a large variety of particles sizes and elemental composition: Be, C, O, Ni+Cr+Fe, Al, W, Mo. Priority has been given to the search for Be-containing objects. SEM images and corresponding EDX spectra in Fig. 17 give an overview of the Be-based particles vacuumed from the divertor after the ILW-2 phase. Four categories of particles have been identified: (i) droplets of molten Be from limiters covered by deposited species (W in this case), thus suggesting their residence in the divertor for some time before the end of the campaign (Fig. 17a); (ii) splashes of the same origin (Fig. 17b); (iii) co-deposits detached from the divertor tiles (Fig. 17c); and (iv) debris of Be from the tiles (Fig. 17d) – however, the origin of such debris is most probably associated with the installation of PFC by the remotely handled (RH) robotic arm.

Another topic has been related to the tritium presence in different types of particles. Detailed examination was preceded by the selection process using imaging plate (IP) technique to identify tritium-free and tritium-containing particles. It has been noticed that Be particles contain much less tritium than in carbon and even in tungsten grains [307].

Local sampling by adhesive carbon stickers and by in-vessel dust monitors revealed a large diversity of collected particles. Material sampled by adhesive sticky pads is dominated by pieces of Be-rich co-deposits as reported in Refs. [301,302,306]. There is also a very limited amount of flakes detached from the Be-coated tiles of the inner wall cladding (just one detected) and small Be droplets are also detected [302]. A characteristic feature described in detail in Refs. [300,302] is related to significant structural differences of Be-rich co-deposits: from compact and dense stratified structures to very loose matter with porosity exceeding 50%, as could be estimated from focused ion beam (FIB) -produced and STEM-examined samples. Porous co-deposits resemble nano-tubes and their density was assessed to be on the order of about 0.6 $gcm^{-3}$ [300].

Particles found on the dust monitor Si plates represent material which was not mechanically disturbed by the collection method, as unavoidably happens in the case of vacuum cleaning or sampling with sticky pads. A variety of dust particles and also Be-rich co-deposits resulting from material migration in JET-ILW [300] are found. The 300–350 nm thick layer formed on the Si plate tends to flake due to the internal stress related to thermo-mechanical incompatibility at the Si-deposit interface. Blisters, 4–60 µm in diameter, are observed which break and peel-off, but fragments of those flakes have not been detected on the monitor. On the contrary, particles deposited on the monitor stick well to the surface. Their areal density amounts to approx. 400–500 $cm^{-2}$, as estimated from SEM survey images.

Be on dust monitors and also on other wall probes occurs in the form of circular flat splashes (Fig. 18a, b) and droplets of regular spherical or oval shape (Fig. 18c, d), while elongated particles are very rare objects (Fig. 18e). This fairly regular shape and only traces of co-deposit on the surface of splashes indicate that they were formed in the very last stage of the second operational period of JET-ILW (ILW-2), when experiments on runaway electron generation were carried out. This resulted in melting of the upper dump plates and, as a consequence, ejection of molten matter. On the surfaces of many studied Be droplets and splashes nano-bubbles/blisters (100–250 nm in diameter) and pits of similar dimensions are found. Their presence suggests boiling of Be liberated from the limiters (details shown in Refs. [300,303]).

In summary, all studies of the dust from JET-ILW have consistently shown that the amount of Be-rich particles was very small. Their fraction may be conservatively estimated at the level of 1–2% of the total number of particles retrieved from the machine. It is also very strongly stressed that Be splashes adhere well to the substrates on which they are deposited, thus showing that the release of molten metal cannot be directly translated to the formation of loose matter, i.e. easily mobilizable Be particles. Risks related to potential dust mobilization during the RH in-vessel operation is a safety concern. Therefore, a dedicated experiment was performed in JET-ILW. Ten dust collectors (sticky pads) was placed at various locations on the RH robotic arm. The accumulation of Be- and W-based particles was negligible: only a single particle of Be-rich deposit was identified. The study confirmed earlier experimental evidence that Be-rich co-deposits (and also W coatings on CFC) adhere well to PFC surfaces. The absolute majority of collected objects were aluminium-based and most likely originated from the construction material of the RH equipment itself [310].

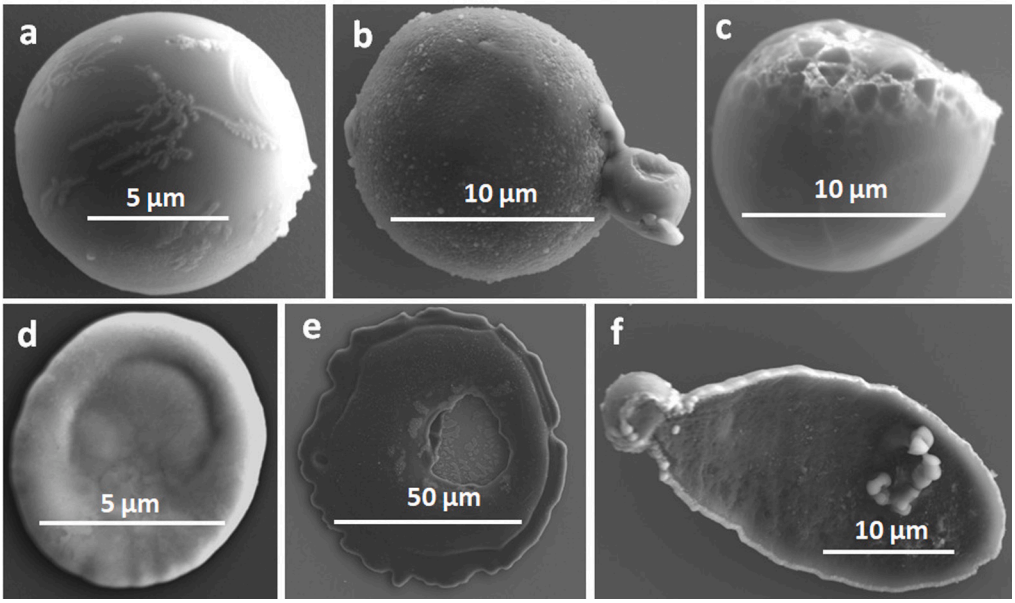


**Fig. 18.** Be droplets (a–c) and splashes (d–f) found on dust monitors during ILW-2.

## 6. Fundamental simulations of hydrogen behaviour in Be

### *6.1. Electronic structure calculations for hydrogen trapping and migration in Be*

First-principle calculations based on electronic density functional theories (DFT) studying H trapping and migration in Be have been published in Refs. [311–316]. Recently, the available data were critically reviewed and the discrepancies, as well as some additional data needs, were identified [317]. In a recent project [317,318], the main thermodynamic and kinetic parameters for H in Be were re-evaluated and the data set was extended. The main results and conclusions are described here.

The diffusion of mono-vacancies in Be is found to be anisotropic with lower activation energy (0.66 eV) in the basal plane of the hexagonal close-packed (hcp) crystal than out of the basal plane (0.83 eV). The Be self-interstitial atom diffusion is likewise anisotropic with lower activation energies in the basal plane (0.12 eV) than out of it (1.08 eV). In addition, for the Be self-interstitials there also exists a path with an activation energy of only 0.29 eV, which involves migration both in and out of plane. The diffusion of solute hydrogen in non-defective Be is an isotropic 2-step process involving migration between basal-tetrahedral (BT) and octahedral (O) positions with the total activation energy of 0.39 eV (BT→BT) and intermediate minima at O-positions with 0.19 eV energy barriers (O→BT). According to DFT calculations, up to 5 H atoms can be trapped in a single Be mono-vacancy with the detrapping energies gradually decreasing with occupancy from about 1.5 eV for single H occupancy ($H_1$-V) down to about 1.0 eV for the maximal occupancy of 5 H atoms ($H_5$-V). The calculated detrapping energy barriers are calculated for migration from the vacancy to one of the second nearest neighbour BT positions. These results represent the first calculations of H migration paths near Be vacancies for all vacancy occupancies, and hence provide detailed energy landscapes around vacancies governing the trapping and de-trapping processes. The Be di-vacancies were found to be energetically unfavourable for binding and therefore unstable. However, the di-vacancies can be stabilized by trapping of H atoms, thus providing a potential mechanism for vacancy clustering and subsequent void formation.

Hydrogen diffusion and retention in Be compounds has been studied with DFT for tungsten beryllide ($Be_{12}W$) [319], beryllium oxide (BeO) [320] and beryllium nitride ($\alpha$-$Be_3N_2$) [321]. In the $Be_{12}W$ lattice four different atomistic structures can be identified depending on their geometries with different H formation energies, which is attributed to interstitial positions around atoms of each type. The dissolution energy of an interstitial H atom lies between 1.10 eV and 1.41 eV (with zero-point energy correction). These values fall between H dissolution energy 1.05 eV in a pure W metal and 2.20 eV in a pure Be metal. The H atom was found to diffuse without barrier along the sublattice formed by the W atoms. H migration from the W sublattice to the Be sublattice, and between different types of Be atoms exhibits an activation energy of 0.3–0.5 eV depending on the process type and direction. Multiple trapping of H in different types of single vacancies corresponding to different types of missing atoms in the $Be_{12}W$ lattice was calculated in Ref. [319]. The detrapping energies vary in the range from 0.8 eV down to about 0.45 eV for a W-vacancy depending on the H occupancy. For different types of Be-vacancies the detrapping energies were found to decrease from about 1 eV~1.3 eV down to about 0.5 eV~0.9 eV depending on the occupancy.

For BeO, the DFT calculations predict strong anisotropy for diffusion of self-interstitial Be atoms (1.9 eV and 0.9 eV) and self-interstitial O atoms (1.09 eV and 1.43 eV) [320]. The diffusion of solute H is anisotropic with activation energies 0.88 eV and 0.7 eV, whereas it was found to be strongly trapped by Be- and O-vacancies with detrapping energies of 2.87 eV and 3.44 eV, respectively.

In $\alpha$-$Be_3N_2$, three different interstitial sites were identified, which were associated to bonding with neighbouring Be atoms or with two types of N atoms that have different chemical environment [321]. H was found to have migration paths from a Be trapping site to an N trapping site and back, between Be sites and between N sites with activation energies of 0.41–0.66 eV depending on the particular path. Further, H is strongly trapped in Be- and N-vacancies with detrapping energies of 2.47 eV and 3.42 eV, respectively.

### *6.2. Long timescale evolution simulations*

#### *6.2.1. Molecular dynamics simulations of erosion and deposition of Be*

The erosion and surface morphology of clean bulk Be has been studied computationally using the MD technique. Simulations comprise of cumulative D irradiations scanning over different irradiation parameters, such as irradiation energy, particle flux, target temperatures, and formation and release of $BeD_n$ molecules. Fig. 19 summarizes the main findings on total Be sputtering by D as obtained with MD [322]. At

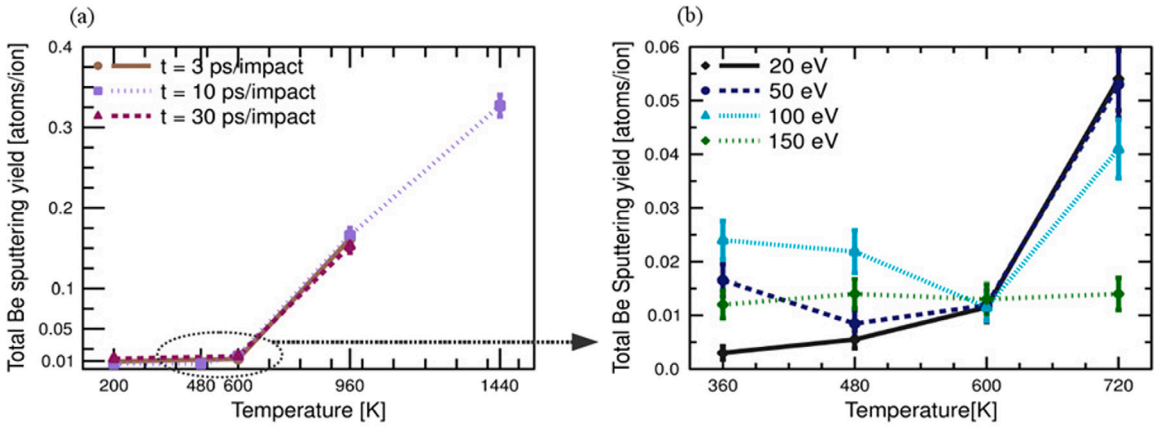


**Fig. 19.** Molecular dynamics simulation results for total Be sputtering yield by D (N = 2000). (a) Constant D impact energy 50 eV with varying D fluxes and Be surface temperatures. Time intervals (in ps) between D particles bombarding the Be surface 3, 10 and 30 ps correspond to fluxes $6.73\times10^{24}$, $2.02\times10^{24}$ and $0.67\times10^{24}$ $cm^{-2}s^{-1}$, respectively. (b) Constant D flux of 10 ps/impact ($2.02\times10^{24}$ $cm^{-2}s^{-1}$) with varying D energies and JET-ILW surface temperatures.
*Source:* Reproduced from Ref. [322].

600 K, the implanted D atoms migrate back to the surface, ending up mostly bound to Be atoms. At this temperature range, D could be easily desorbed when forming $D_2$ molecules, increasing the fraction of D released in molecular form. The highest temperature, 1440 K, is close to the Be melting point, leading to an increased Be sputtering due to the increased atomic vibrational energy that weaken the interatomic bonding of Be at high temperatures. With increasing temperature, the Be sputtering yield increased at low impact energies (<150 eV).

In general, the Be surface morphology showed significant change at different surface temperatures under D irradiation with different energies. The Be surface damage was initiated already at the very beginning of each D bombardment simulation. The implanted D was found to bond with the Be atoms, and the deposited D-induced surface modification at higher temperatures. Moreover, the erosion was not homogeneous, leading to surface roughening.

The molecular erosion showed strong temperature dependence. Elevated temperature has an effect on the topmost surface D concentration and on the resulted $BeD_n$ formation as shown in Ref. [322]. At temperatures lower than 500 K, the implanted D resides in the bulk subsurface region resulting in low D concentration at the topmost surface layer and consequently in low molecular erosion, where the main eroded molecular species was seen to be BeD. At higher temperatures (T ≈ 600 K), the D surface concentration increased due to the increased D diffusion from bulk to surface, which resulted in a rapid increase in total sputtering yield of Be atoms and $BeD_2$ and $BeD_3$ molecules became the main eroded species, reducing the sputtered BeD:Be fraction. At even higher temperatures (T > 1000 K), the Be was eroded again in atomic form and as BeD molecules.

Fig. 20 presents a comparison of the MD simulated and experimentally measured total Be sputtering yields at the PISCES-B facility for 300 K surface temperature as a function of the incident D ion energy. The experimental PISCES-B yields were measured using a polycrystalline Be sample [323]. The difference between the MD and experimental total Be yields is considerable, especially for impact energies higher than 60 eV. However, the experimental yield follows a similar increasing trend as is seen in the MD simulations.

The effect of vacancy concentrations on the long-range D retention in the bulk region of Be was studied with OKMC calculations using the MD results [290]. Vacancies are more favourable defects to accommodate D atoms than the interstitial sites in Be; therefore, a higher vacancy concentration provides more traps in which D atoms can be accommodated and hence higher D concentrations. According to the OKMC results, a linear correlation of the D distribution with vacancy concentration was observed. At higher temperatures, the D atoms distribute more evenly and deeper in the material, yielding to D surface content decrease with increasing temperature. The key finding obtained with OKMC is the strong temperature dependency of the D concentration with the number of vacancies. In the initial stage all vacancies were found to be filled with up to 5 D atoms ($D_5$-V) and the other incoming D atoms from the irradiations diffused within the material as interstitials. At lower temperatures, the D atoms remain in the vacancies and form immobile $D_5V$ defects. At higher temperatures, the probability of D atoms becoming detrapped from the vacancies increases due to the low D binding energy, and the detrapped D diffuse fast towards the surface or deeper in the bulk as an interstitial.

The present MD simulations confirm the experimentally observed reduction of sputtered BeD molecules with increasing target temperature and with increasing D ion impact energy (Fig. 20). This is seen as a linear decrease in the ratio of the sputtered species BeD:Be, as reported by experiments done at PISCES and JET (Section 5.1). Thus, the MD results provide a detailed database of erosion yields to the large scale impurity transport codes, such as ERO (Section 5.2).

Moreover, the resulting Be erosion yields were found to increase in the presence of Ar and Ne plasma impurities in comparison with pure D irradiation [324]. The sputtering yields increased with increasing impact energy, while the effect of substrate temperature was found to be negligible. The effect of impurities on $BeD_n$ molecular sputtering is less significant and most of the sputtered species were BeD molecules. At impact energies lower than 50 eV, adding noble gas impurities to D bombardments would not significantly affect the Be erosion yield. Furthermore, the sputtering mechanism at low ion irradiation energy is due to the swift chemical sputtering, or CAPS phenomenon, which means that Ar and Ne have very low probabilities of causing swift chemical sputtering. However, noble gases affect the total erosion of Be targets at impact energies higher than 100 eV where the possibility for pure physical sputtering increases.

### 6.2.2. *Calculations with rate theory equations*

Measurements using TDS (Sections 3.1 and 3.3.3) are usually applied to study the total retention of gaseous species (mainly hydrogen isotopes), as well as the presence of their different binding states in the material. In the case in which different isotopes are present, heterogeneous molecules are also measured (e.g. HD or DT). Although classically applied to surface adsorbates, TDS is also widely used to study hydrogen release from the bulk material. The release dynamics can differ for H, D and T isotopes and happen also in form of molecules (for instance $D_2$), and thus are dependent on the recombination of atoms at the surface. In this case the release is governed not only by desorption from the surface, but also by diffusion towards the surface,

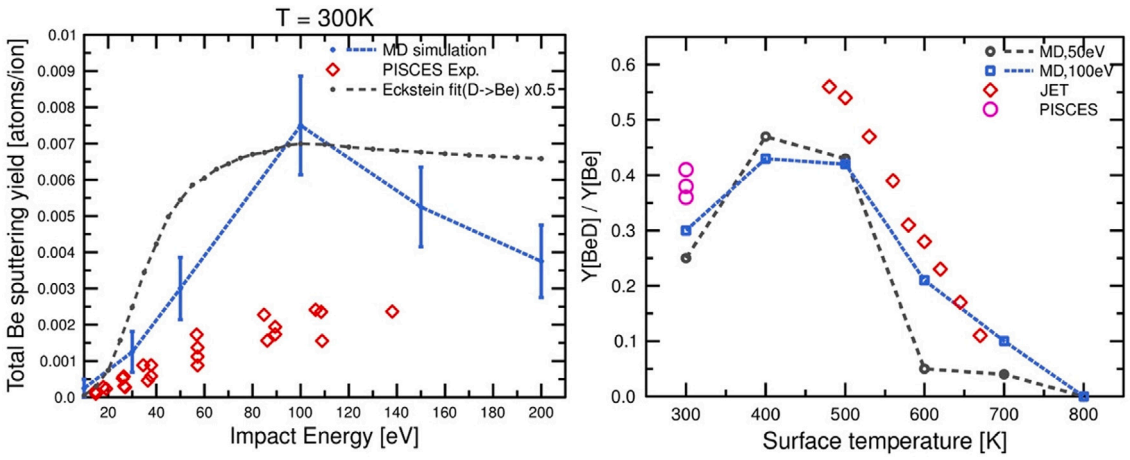


**Fig. 20.** Left: Comparison of simulated (MD) and experimental (PISCES-B) results of total Be sputtering yield as a function of D impact energy at a 300 K surface temperature. The corresponding Eckstein fit also shown (×0.5). Right: Comparison of the sputtered BeD:Be ratios obtained by two different MD approaches and experiments done at JET-ILW and PISCES-B as a function of surface temperature.
*Source:* Reproduced from Ref. [290].

which, in turn, is often limited by multiple events of trapping and de-trapping in the material defects happening on the way to the surface. The latter process is dependent on the density of defects of various types. Since analysis of the time and temperature evolution of release is possible only in a limited number of cases, modelling is usually applied to interpret the measurements.

In reaction–diffusion codes, systems of coupled partial differential equations (PDE) describing the time evolution of volume concentrations of mobile and trapped species within the material are solved in order to reproduce the course of a particular TDS experiment. The typical processes taken into account in such a model are the diffusive transport and the reactions of trapping and de-trapping into/out of different trapping sites (defects) in the material. A time dependent desorption flux from the surface as a function of near-surface hydrogen concentration can be introduced as a boundary condition for the problem. Additional terms, such as implantation sources and transformation reactions can be added depending on the physical system under consideration. As a result of such a simulation, the time evolution of the volume concentration of hydrogen (trapped and solute) is obtained and the desorption flux of particular species, e.g. $D_2$, can be compared to the corresponding experimental data.

By adjusting the parameters of the model, such as diffusion constants and de-trapping energy barriers, experimental TDS spectra can be fitted, providing information on particular mechanisms of particle binding and migration in the material, which are otherwise not decipherable from the global measurement. Ab initio calculations, such as DFT (Section 6.1), provide fundamental data points, however these cannot cover all the needs, thus some values have to be treated as free parameters, which provide effective reference values for particular parameters (normally these are diffusion and de-trapping activation energies). Several established reaction–diffusion codes for fusion applications exist, such as TMAP7 [326], advanced RE [327], TESSIM [328], WHIMS [329], FESTIM [330] and CRDS [325]. These codes are typically one-dimensional, but recent efforts have been made to develop 2D and 3D codes able to study the influence of the complex PFC geometry on retention and permeation [331].

In the following, an example on the application of a reaction–diffusion code is given. Coupled Reaction–Diffusion Systems (CRDS) [325] is a reaction–diffusion code, which is applied to analysis of TDS experiments on ion beam implanted single-crystalline Be [332–334], and to desorption experiments on Be/D co-deposited layers [335]. Recently, this code has been optimized and extended to include, in particular, multiple-trapping in mono-vacancies, surface coverage dependent desorption, and the formation of di-vacancies [325,336]. The most recent set of DFT data [317] is used as input for the code.

CRDS has been applied to model TDS experiments on single-crystal Be implanted by 1 keV D atoms with different fluences. D trapping in implantation-induced mono-vacancies in Be is found to be the main retention mechanism at low D fluences. The retention increases linearly with the fluence up to about $5 \times 10^{20}$ $m^{-2}$ due to the increase in the number of implantation-produced trapping sites (vacancies). According to experimental data, in the fluence range $(0.5–1.5) \times 10^{21}$ $m^{-2}$ the amount of implantation-produced vacancies saturates, potentially due to defect annealing during irradiation. This leads to broadening of the TDS release peak towards higher temperatures and formation of a shoulder at the lower temperature side (Fig. 21). These modifications are attributed to trapping of more than three D atoms per mono-vacancy, as well as to possible vacancy clustering (vacancy clusters stabilized by D trapping, Section 6.1). In addition, an extension of the D retention region deeper into the bulk Be can be responsible for the observed peak broadening towards higher temperature.

At fluences greater than $1.5 \times 10^{21}$ $m^{-2}$ the sudden formation of a low temperature peak in the TDS spectrum is observed, which was earlier [332] attributed to amorphization and formation of hydride phases in Be. CRDS simulations indicate qualitatively that formation of the low temperature binding states of D can be attributed to D accumulation on the surface of Be, as the number of vacancies in the bulk gets saturated. The surface coverage dependent desorption barrier allows saturation of total D retention in Be due to release from the saturated surface during ion beam exposure. It is pointed out in Refs. [325,336], however, that a factor 10 larger surface area has to be assumed to reproduce the experimental peak height, thus suggesting development of a porous surface structure during exposure. At the same time, formation of gas filled voids via vacancy clustering could contribute to the appearance of low energy binding states.

## 7. Concluding remarks

This work provides a comprehensive overview and literature survey on the application and properties of beryllium in nuclear fusion devices, and updates the information published previously [3,4]. The preparation of such a review has also allowed the identification of gaps and critical issues to be addressed in depth by future research to improve predictive capabilities for ITER. One important area, as mentioned in the Introduction (Section 1), is the impact of neutron-induced damage on material structure and fuel retention. Most probably, it will not be a subject of a quickly achieved resolution because of the current lack of a relevant fusion neutron source. In this case, ion-induced damage to simulate neutron effects may lead to answers with a high level of

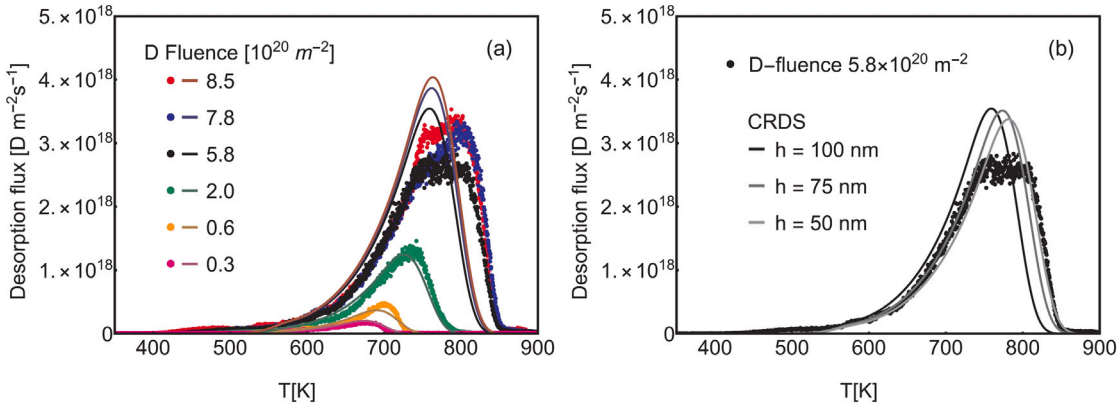


**Fig. 21.** An example of CRDS simulations of TDS spectra obtained after 1 keV/D implantation in single-crystalline Be (a) at different implantation fluences, and (b) for fluence $5 \times 10^{20}$ $Dm^{-1}$, but with varying the initial D depth profile (h) parameter. See text for more details.
*Source:* Reproduced from Ref. [325].

uncertainty. However, an outstanding aspect which requires neutrons is the activation of Be PFCs, and equally crucial is the activation of intrinsic trace impurity species, such as uranium [337] which can lead to the formation of plutonium. Material purity certificates with a list of trace impurities is a pre-requisite, while such neutron experiments could also be recommended in the materials qualification process.

Two other areas are related to Be limiters from JET-ILW: (i) the impact of the chemical state of Be surfaces on fuel retention; (ii) the consequences of the damage by power loads on fuel retention. Relevant materials have been retrieved from JET-ILW and their characterization has begun. Their chemical state has been determined using surface Raman spectroscopy [338] while metallography and mechanical studies of limiters have provided the first data on the surface, subsurface and bulk state in areas heavily affected by the plasma [339]. This will be followed by retention studies. The JET-ILW results have confirmed that the tritium retention in ITER will be dominated by co-deposition of tritium with Be eroded from the first wall. While significant progress has been made to understand the retention properties of Be co-deposits produced in laboratory experiments and to provide predictive capabilities for ITER in terms of the amount of retention, much remains to be done. A comparison between deuterium desorption from Be co-deposits formed in JET and in PISCES-B has shown [223,340] similarities and differences in the D trapping properties. The physical processes causing trapping in co-deposits are still rather unclear. In particular, JET co-deposits contain more impurities, such as historical carbon originating from the JET-C era, than the co-deposits produced in the laboratory. While co-deposits in ITER will also contain some level of impurities, it is expected that the level of observed carbon will be lower than in JET. Computer modelling of the co-deposition process carried out with e.g. MD simulations, is necessary to shed some light on the fundamentals of the trapping processes and how they depend on the local co-deposition conditions. This is required to understand and predict the efficiency of tritium removal by baking in ITER.

Another challenge for ITER is an improved understanding of Be dust formation and its properties. Only microscopic amounts of loose matter is collected from the whole divertor region of JET after each JET-ILW operational campaign: the total amount of collected material is of the order of ~1 gram per campaign, which includes plasma disruptions and steady-state operations. Of this collected material, loose Be amounts to just tens of milligrammes [272,300,341]. This makes the determination of the size distribution and the surface specific area – two important parameters for ITER – extremely difficult and inconclusive taking into account the possible disintegration of particles during collection process by RH vacuum cleaner. Serious safety risks may be related to the instability of otherwise well-adhered co-deposits in accidents involving moisture (water, vapour) ingress to the machine. Early results of dedicated experiments carried out with Be limiters from JET-ILW do not indicate dust generation under direct exposure to hot water [342,343]. However, it has been observed that Be layers deposited by magnetron sputtering had a very low adhesion on tungsten substrates, and the substrates had to be significantly roughened to ensure some adhesion [195]. More studies on layer adhesion and mechanical stability of Be layers are needed. Ejection of metal droplets during disruptions is thought to be a key mechanism for dust creation in ITER. A further crucial issue for ITER is to understand the possibility of Be splashing during transient events and to quantify the amount of material which could be ejected from the molten surface.

An important aim of activities in JET-ILW and PISCES-B is to provide data to modellers, both to validate transport codes and interpret material migration scenarios and their impact on fuel retention. A significant transport of Be to shadowed areas of the JET divertor is measured [190,247,300]. The mechanism of this transport needs to be identified: a key question refers to the role of CAPS, and therefore of molecular species, on material migration. To date there is no clear evidence of this, which indicates that molecular species probably are dissociated very quickly, hence making their role in long-range material migration less significant, but this needs to be verified.

## Acknowledgements

This article forms the final report of an IAEA Coordinated Research Project F43020 entitled “Data for Erosion and Tritium Retention in Beryllium Plasma-Facing Materials". Part of this work has been carried out within the framework of the EUROfusion Consortium and which has received funding from the Euratom research and training program 2014–2018 and 2019–2020 under grant agreement No. 633053. The views and opinions expressed herein do not necessarily reflect those of the European Commission or of the ITER Organization. Part of this work was supported by a grant from the Department of Energy, DE-FG02-07ER54912, and as part of the US-EU Bilateral Collaboration on Mixed Materials for ITER. Part of this work received financial support from the tandem accelerator infrastructure by VR-RFI (contract #2017-00646_9) and from the Swedish Foundation for Strategic Research (SSF) under contract RIF14-005.

DB would like to acknowledge Dmitriy Matveev, Timo Dittmar, Petra Hansen and Rudi Koslowski for their contributions and valuable remarks for the text.

## Declaration of competing interest

The authors declare that they have no known competing financial interests or personal relationships that could have appeared to influence the work reported in this paper.

## References


[1] G. Federici, C.H. Skinner, J.N. Brooks, J.P. Coad, C. Grisolia, A.A. Haasz, A. Hassanein, V. Phillips, C.S. Pitcher, J. Roth, W.R. Wampler, D.G. Whyte, Nucl. Fusion 41 (2001) 1967.
[2] A. Loarte, B. Lipschultz, A.S. Kukushkin, G.F. Matthews, P.C. Stangeby, N. Asakura, G.F. Counsell, G. Federici, A. Kallenbach, K. Krieger, et al., Nucl. Fusion 47 (2007) S203.
[3] J. Roth, E. Tsitrone, A. Loarte, Th. Loarer, G. Counsell, R. Neu, V. Philipps, S. Brezinsek, M. Lehnen, P. Coad, Ch. Grisolia, K. Schmid, K. Krieger, A. Kallenbach, B. Lipschultz, R. Doerner, R. Causey, V. Alimov, W. Shu, O. Ogorodnikova, A. Kirschner, G. Federici, A. Kukushkin, J. Nucl. Mater. 390 (2009) 1.
[4] G. Federici, R. Doerner, P. Lorenzetto, V. Barabash, Compr. Nucl. Mater. 4 (2012) 621.
[5] R.G. Macaulay-Newcombe, D.A. Thompson, J. Nucl. Mater. 212–215 (1994) 942.
[6] M. Mayer, R. Behrisch, H. Plankand, J. Roth, G. Dollinger, C.M. Frey, J. Nucl. Mater. 230 (1996) 67.
[7] R.A. Anderl, G.R. Longhurst, R.J. Pawelko, M.A. Oates, J. Fusion Energy 16 (1997) 95.
[8] K. Ashida, K. Watanabe, T. Okabe, J. Nucl. Mater. 241–243 (1997) 1060.
[9] R.P. Doerner, A. Grossman, S. Luckhardt, R. Seraydarian, F.C. Sze, D.G. Whyte, R.W. Conn, J. Nucl. Mater. 257 (1998) 51.
[10] E. Abramov, M.P. Riehm, D.A. Thompson, W.W. Smeltzer, J. Nucl. Mater. 175 (1990) 90.
[11] R.A. Causey, W.L. Hsu, B.E. Mills, J. Ehrenberg, V. Phillips, J. Nucl. Mater. 176–177 (1990) 218.
[12] R.G. Macaulay-Newcombe, D.A. Thompson, W.W. Smeltzer, Fusion Eng. Des. 18 (1991) 419.
[13] D.A. Thompson R.G. Macaulay-Newcombe, W.W. Smeltzer, J. Nucl. Mater. 191–194 (1991) 419.
[14] R.G. Macaulay-Newcombe, D.A. Thompson, W.W. Smeltzer, J. Nucl. Mater. 191–194 (1992) 263.
[15] W.R. Wampler, J. Nucl. Mater. 196–198 (1992) 981.
[16] Y.M. Zakaria, R.G. Macaulay-Newcombe, D.A. Thompson, Proc. Workshop on Beryllium for Fusion Applications, Kernforschungszentrum Karlsruhe Report KfK 5271, 1993, p. 331.
[17] R.A. Causey, K.L. Wilson, J. Nucl. Mater. 212–215 (1994) 1436.
[18] F. Schiettekatte, D. Keroack, G.G. Ross, B. Terreault, Nucl. Instrum. Methods Phys. Res. B 90 (1994) 401.
[19] D. Kéroack, B. Terreault, J. Nucl. Mater. 212–215 (1994) 1443.
[20] E.A. Denisov, T.N. Kompaniets, A.A. Kurdyumov, S.N. Mazayev, Yu.G. Prokofiev, J. Nucl. Mater. 212–215 (1994) 1448.
[21] V.Kh. Alimov, R.Kh. Zalavutdinov A.E. Gorodetsky, A.P. Zakharov, J. Nucl. Mater. 220–222 (1995) 947.
[22] L. Buisson, P. Bracconi, X. Claudon, Appl. Surf. Sci. 84 (1995) 211.
[23] E. Ishitsuka, H. Kawamura, Y. Hishinuma, M. Nakamura, K. Tatenuma, Fusion Technol. 28 (1995) 647.
[24] R.A. Anderl, J.D. Baker, G.L. Bourne, R.J. Pawelko, Fusion Technol. 28 (1995) 1114.
[25] K. Kizu, K. Miyazaki, T. Tanabe, Fusion Technol. 28 (1995) 1205.
[26] G.R. Longhurst, R.A. Anderl, T.J. Dolan, M.J. Mulock, Fusion Technol. 28 (1995) 1217.
[27] A.A. Pisarev, Fusion Technol. 28 (1995) 1262.
[28] B. Terreault, D. Kéroack, G.G. Ross, R.G. Saint-Jacques, F. Schiettekatte, K. Touhouche, P. Zheng, J. Nucl. Mater. 220–222 (1995) 790.
[29] V.N. Chernikov, V. Kh. Alimov, A.N. Markin, A.P. Zakharov, J. Nucl. Mater. 228 (1996) 47.
[30] V.N. Chernikov, V. Kh. Alimov, A.V. Markin, A.E. Gorodetsky, S.L. Kanashenko, A.P. Zakharov, I.B. Kupriyanov, J. Nucl. Mater. 233 (1996) 860.
[31] I.P. Chernov, Y.P. Cherdantsev, V.G. Abdrashitov, J. Nucl. Mater. 233–237 (1996) 857.
[32] A.V. Markin, V.N. Chernikov, S.Yu. Rybakov, A.P. Zakharov, J. Nucl. Mater. 233–237 (1996) 865.
[33] V.M. Sharapov, L.E. Gavrilov, V.S. Kulikauskas, A.V. Markin, J. Nucl. Mater. 233–237 (1996) 870.
[34] B. Tsuchiya, K. Morita, J. Nucl. Mater. 233–237 (1996) 898.
[35] A.A. Pisarev, M.L. Grachova, J. Nucl. Mater. 233–237 (1996) 1137.
[36] N. Yoshida, S. Mizusawa, R. Sakamoto, T. Muroga, Fusion Technol. 30 (1996) 798.
[37] M.I. Guseva, A.Yu. Birukov, V.M. Gureev, L.S. Daneljan, S.N. Korshunov, Yu.V. Martynenko, P.S. Moskovkin, Yu.A. Sokolov, V.G. Stoljarova, V.S. Kulikauskas, V.V. Zatekin, J. Nucl. Mater. 233–237 (1996) 681.
[38] V.Kh. Alimov, V.N. Chernikov, A.P. Zakharov, J. Nucl. Mater. 241–243 (1997) 1047.
[39] A.A. Haasz, J.W. Davis, J. Nucl. Mater. 241–243 (1997) 1076.
[40] B. Tsuchiya, K. Morita, J. Nucl. Mater. 241–243 (1997) 1065.
[41] K. Morita, B. Tsuchiya, J. Nucl. Mater. 248 (1997) 27.
[42] B. Tsuchiya, K. Morita, J. Nucl. Mater. 248 (1997) 42.
[43] J. Won, F.E. Spada, R. Boivin, R.P. Doerner, S. Luckhardt, F.C. Sze, R.W. Conn, J. Nucl. Mater. 241–243 (1997) 1110.
[44] A.P. Zakharov, A.E. Gorodetsky, V.Kh. Alimov, S.L. Kanashenko, A.V. Markin, J. Nucl. Mater. 241–243 (1997) 52.
[45] R.A. Causey, G.R. Longhurst, W. Harbin, J. Nucl. Mater. 241–243 (1997) 1041.
[46] V.M. Sharapov, V.Kh. Alimov, L.E. Gavrilov, J. Nucl. Mater. 258–263 (1998) 803.
[47] V.M. Sharapov, E. Gavrilov, V.Kh. Alimov, Plasma Dev. Oper. 6 (1998) 89.
[48] A.Yu. Biryukov, D.V. Andreev, S.A. Gavrilov, L.S. Danelian, V.I. Antropovand, S.N. Mazaev, Plasma Dev. Oper. 6 (1998) 259.
[49] G.R. Longhurst, R.A. Anderl, R.A. Causey, G. Federici, A.A. Haasz, R.J. Pawelko, J. Nucl. Mater. 258–263 (1998) 640.
[50] S.P. Vagin, P.V. Chakrov, B.D. Utkelbayev, L.A. Jacobson, R.D. Field, H. Kung, J. Nucl. Mater. 258–263 (1998) 719.
[51] R.A. Causey, D.S. Walsh, J. Nucl. Mater. 254 (1998) 84.
[52] R.A. Causey, J. Nucl. Mater. 300 (2002) 91.
[53] G. Federici, R. Anderl, J.N. Brooks, R. Causey, J.P. Coad, D. Cowgill, R.P. Doerner, A.A. Haasz, G. Longhurst, S. Luckhardt, D. Mueller, A. Peacock, M. Pick, C.H. Skinner, W. Wampler, K. Wilson, C. Wong, C. Wu, D. Youchison, Fusion Eng. Des. 39–40 (1998) 445.
[54] V.Kh. Alimov, V.N. Chernikov, J. Nucl. Mater. 273 (1999) 277.
[55] J. Won, R.P. Doerner, R.W. Conn, J. Nucl. Mater. 256 (1998) 96.
[56] A.V. Markin, V.P. Dubkov, A.E. Gorodetsky, M.A. Negodaev, N.V. Rozhanskii, F. Scafidi-Argentina, H. Werle, C.H. Wu, R.Kh. Zalavutdinov, A.P. Zakharov, J. Nucl. Mater. 283–287 (2000) 1094.
[57] A.P Zakharov, A.E. Gorodetsky, V.Kh. Alimov, Russ. J. Inorg. Chem. 47 (2002) 552.
[58] A.M. Zimin, M.I. Guseva, N.G. Elistratov, L.S. Danelyan, V.M. Gureev, B.N. Kolbasov, V.S. Kulikauskas, V.G. Stolyarova, N.N. Vasiliev, V.V. Zatekin, Plasma Dev. Oper. 12 (2004) 89.
[59] C.H. Skinner, A.A. Haasz, V.Kh. Alimov, N. Bekris, R.A. Causey, R.E.H. Clark, J.P. Coad, J.W. Davis, R.P. Doerner, M. Mayer, A. Pisarev, J. Roth, T. Tanabe, Fusion Sci. Technol. 54 (2008) 891.
[60] G. De Temmerman, M.J. Baldwin, R.P. Doerner, D. Nishijima, K. Schmid, Nucl. Fusion 48 (2008) 075008.
[61] G. De Temmerman, R.P. Doerner, Nucl. Fusion 49 (2009) 042002.
[62] A. Anghel, C. Porosnicu, M. Badulescu, I. Mustata, C.P. Lungu, K. Sugiyama, S. Lindig, K. Krieger, J. Roth, A. Nastuta, G. Rusu, G. Popa, Nucl. Instrum. Methods Phys. Res. B 267 (2009) 426.
[63] R.P. Doerner, M.J. Baldwin, G. De Temmerman, J. Hanna, D. Nishijima, J. Roth, K. Schmid, G.R. Tynan, K. Umstadter, Nucl. Fusion 49 (2009) 035002.
[64] S. Brezinsek, T. Loarer, V. Philipps, H.G. Esser, S. Grünhagen, R. Smith, R. Felton, J. Banks, P. Belo, A. Boboc, J. Bucalossi, M. Clever, J.W. Coenen, I. Coffey, S. Devaux, D. Douai, M. Freisinger, D. Frigione, M. Groth, A. Huber, J. Hobirk, S. Jachmich, S. Knipe, K. Krieger, U. Kruezi, S. Marsen, G.F. Matthews, A.G. Meigs, F. Nave, I. Nunes, R. Neu, J. Roth, M.F. Stamp, S. Vartanian, U. Samm, Nucl. Fusion 53 (2013) 083023.
[65] K. Heinola, A. Widdowson, J. Likonen, E. Alves, A. Baron-Wiechec, N. Barradas, S. Brezinsek, N. Catarino, P. Coad, S. Koivuranta, S. Krat, G.F. Matthews, M. Mayer, P. Petersson, JET Contributors, Phys. Scr. T 167 (2016) 014075.
[66] J.C. Nicoitd, J. Delaplace, J. Hillairet, D. Schumacher, Y. Adda, J. Nucl. Mater. 27 (1968) 147.
[67] J. Delaplace, J.C. Nicoitd, D. Schumacher, G. Vogl, 29 (1968) 819.
[68] M. Dalle Donne, F. Scaffidi-Argentina, C. Ferrero, C. Ronchi, J. Nucl. Mater. 212–215 (1994) 954.
[69] D.L. Baldwin, M.C. Billone, J. Nucl. Mater. 212–215 (1994) 948.
[70] F. Scaffidi-Argentina, M. Dalle Donne, C. Ferrero, C. Ronchi, Fusion Eng. Des. 27 (1995) 275.
[71] S. Cho, M.A. Abdou, Fusion Eng. Des. 28 (1995) 265.
[72] M.A. Lomidze, A.E. Gorodetsky, A.P. Zakharov, Fusion Technol. 28 (1995) 1211.
[73] S.L. Kanashenko, A.E. Gorodetsky, A.P. Zakharov, W.R. Wampler, Phys. Scr. T 64 (1996) 36.
[74] H. Kwast, H. Werle, C.H. Wu, Phys. Scr. T 64 (1996) 41.
[75] D.V. Andreev, V.N. Bespalov, A.Ju. Birjukov, B.A. Gurovich, P.A. Platonov, J. Nucl. Mater. 233–237 (1996) 880.
[76] A.Kh. Klepikov, I.L. Tazhibaeva, V.P. Shestakov, O.G. Romanenko, Y.V. Chikhray, E.A. Kenzhin, Yu.S. Cherepnin, L.N. Tikhomirov, J. Nucl. Mater. 233–237 (1996) 837.
[77] F. Scaffidi-Argentina, M.D. Dalle Donne, C. Ronchi, C. Ferrero, Fusion Technol. 32 (1997) 179.
[78] A.Kh. Klepikov, I.L. Tazhibaeva, O.G. Romanenko, Y.V. Chikhray, V.P. Shestakov, E.A. Kenzhin, J. Nucl. Mater. 258–263 (1998) 798.
[79] F. Scaffidi-Argentina, M.D. Dalle Donne, C. Ronchi, C. Ferrero, Fusion Technol. 33 (1998) 146.
[80] I.L. Tazhibaeva, A.Kh. Klepikov, V.P. Shestakov, O.G. Romanenko, Y.V. Chikhray, E.A. Kenzhin, Yu.S. Cherepninand, L.N. Tikhomirov, Plasma Dev. Oper. 6 (1998) 251.
[81] I.B. Kupriyanov, V.V. Vlasov, Fusion Technol. 38 (2000) 350.
[82] E. Ishitsuka, H. Kawamura, T. Terai, S. Tanaka, J. Nucl. Mater. 283–287 (2000) 1401.

[83] V. Barabash, G. Federici, M. Rödig, L.L. Snead, C.H. Wu, J. Nucl. Mater. 283–287 (2000) 138.
[84] F. Scaffidi-Argentina, C. Sand, C.H. Wu, J. Nucl. Mater. 290–293 (2001) 211.
[85] F. Scaffidi-Argentina, Fusion Eng. Des. 58–59 (2001) 641.
[86] V.P. Chakin, V.A. Kazakov, A.A. Teykovtsev, V.V. Pimenov, G.A. Shimansky, Z.E. Ostrovsky, D.N. Suslov, R.N. Latypov, S.V. Belozerov, I.B. Kupriyanov, Fusion Eng. Des. 58–59 (2001) 535.
[87] E. Rabaglino, C. Ferrero, J. Reimann, C. Ronchi, T. Schulenberg, Fusion Eng. Des. 61–62 (2002) 769.
[88] E. Rabaglino, J.P. Hiernaut, C. Ronchi, F. Scaffidi-Argentina, J. Nucl. Mater. 307–311 (2002) 1424.
[89] M. Uchida, E. Ishitsuka, H. Kawamura, J. Nucl. Mater. 307–311 (2002) 653.
[90] F. Scaffidi-Argentina, G. Piazza, R. Rolli, Fusion Eng. Des. 69 (2003) 505.
[91] I.B. Kupriyanov, V.A. Gorokhov, V.V. Vlasov, A.M. Kovalev, V.P. Chakin, J. Nucl. Mater. 329–333 (2004) 809.
[92] P. Kurinskiy, A. Cardella, M. Klimiankou, A. Möslang, A.A. Goraieb, Fusion Eng. Des. 75–79 (2005) 709.
[93] I.B. Kupriyanov, G.N. Nikolaev, V.V. Vlasov, A.M. Kovalev, V.P. Chakin, J. Nucl. Mater. 367–370 (2007) 511.
[94] N. Nankov, T. Troev, L. Petrov, E. Popov, Nucl. Instrum. Methods Phys. Res. B 266 (2008) 3392.
[95] A. Schmidt, I. Uytdenhouwen, W. Kühnlein, M. Rödig, J. Linke, T. Hirai, G. Pintsuk, Fusion Eng. Des. 83 (2008) 1108.
[96] A. Möslang, R.A. Pieritz, E. Boller, C. Ferrero, J. Nucl. Mater. 386–388 (2009) 1052.
[97] R.D. Plummer, W.L. Gordon, Phys. Rev. Lett. 13 (1964) 432.
[98] E. Jensen, R.A. Bartynski, T. Gustafsson, E.W. Plummer, M.Y. Chou, M.L. Cohen, G.B. Hoflund, Phys. Rev. B 30 (1984) 5500.
[99] E. Jensen, R.A. Bartynski, T. Gustafsson, E.W. Plummer, Phys. Rev. Lett. 52 (1984) 2172.
[100] R.A. Bartynski, E. Jensen, T. Gustafsson, E.W. Plummer, Phys. Rev. B 32 (1985) 1921.
[101] E.W. Plummer, Phys. Scr. T 17 (1987) 186.
[102] J.B. Hannon, E.W. Plummer, R.M. Wentzcovitch, P.K. Lam, Surf. Sci. 269–270 (1992) 7.
[103] H.L. Davis, J.B. Hannon, K.B. Ray, E.W. Plummer, Phys. Rev. Lett. 68 (1992) 2632.
[104] J.B. Hannon, E.W. Plummer, J. Electron Spectrosc. Relat. Phenom. 64–65 (1993) 2632.
[105] E.W. Plummer, J.B. Hannon, 46 (1994) 149.
[106] H.I.P. Johansson, L.I. Johansson, E. Lundgren, J.N. Andersen, R. Nyholm, Phys. Rev. B 49 (1994) 17460.
[107] L.I. Johansson, H.I.P. Johansson, E. Lundgren, J.N. Andersen, R. Nyholm, Surf. Sci. 321 (1994) L219.
[108] R. Stumpf, J.B. Hannon, P.J. Feibelman, E.W. Plummer, Proc. 134th WE-Heraeus Seminar, World Scientific Publishing Company, Singapore, 1995.
[109] L.I. Johansson, Surf. Rev. Lett. 2 (1995) 225.
[110] L.I. Johansson, H.I.P. Johansson, Nucl. Instrum. Methods Phys. Res. B 97 (1995) 430.
[111] P. Hofmann, R. Stumpf, V.M. Silkin, E.V. Chulkov, E.W. Plummer, Surf. Sci. 355 (1996) L278.
[112] P. Hofmann, K. Pohl, R. Stumpf, E.W. Plummer, Phys. Rev. B 53 (1996) 13715.
[113] J.B. Hannon, K. Pohl, P.J. Rous, E.W. Plummer, Surf. Sci. 364 (1996) L617.
[114] J.B. Hannon, E.J. Mele, E.W. Plummer, Phys. Rev. B 53 (1996) 2090.
[115] B.G. Briner, Ph. Hofmann, M. Doering, H.-P. Rust, E.W. Plummer, A.M. Bradshaw, Europhys. Lett. 39 (1997) 67.
[116] P.T. Sprunger, L. Petersen, E.W. Plummer, E. Laegsgaard, F. Besenbacher, Science 275 (1997) 1764.
[117] P. Hofmann, E.W. Plummer, Surf. Sci. 377–379 (1997) 330.
[118] P. Hofmann, B.G. Briner, M. Doering, H.-P. Rust, E.W. Plummer, A.M. Bradshaw, Phys. Rev. Lett. 79 (1997) 265.
[119] L.I. Johansson, P.-A. Glans, T. Balasubramanian, Phys. Rev. B 58 (1998) 3621.
[120] B.G. Briner, Ph. Hofmann, M. Doering, H.-P. Rust, E.W. Plummer, A.M. Bradshaw, Phys. Rev. B 58 (1998) 13931.
[121] S. Lizzit, K. Pohl, A. Baraldi, G. Comelli, V. Fritzsche, E.W. Plummer, R. Stumpf, Ph. Hofmann, Phys. Rev. Lett. 81 (1998) 3271.
[122] K. Pohl, J.-H. Cho, K. Terakura, M. Scheffler, E.W. Plummer, Phys. Rev. Lett. 80 (1998) 2853.
[123] J.-H. Cho, K.S. Kim, S.-H. Lee, M.-H Kang, Z. Zhang, Phys. Rev. Lett. 61 (2000) 9975.
[124] Ismail, Ph. Hofmann, A.P. Baddorf, E.W. Plummer, Phys. Rev. B 66 (2002) 245414.
[125] S.-J. Tang, Ismail, P.T. Sprunger, E.W. Plummer, Phys. Rev. B 65 (2002) 235428.
[126] A. Baraldi, S. Lizzit, K. Pohl, P. Hofmann, S. de Gironcoli, Europhys. Lett. 64 (2003) 364.
[127] J. Rundgren, Phys. Rev. B 68 (2003) 125405.
[128] C.Q. Sun, B.K. Tay, Y.Q. Fu, S. Li, T.P. Chen, H.L. Bai, E.Y. Jiang, J. Phys. Chem. B 107 (2003) 411.
[129] C.Q. Sun, Phys. Rev. B 69 (2004) 045105.
[130] P.-A. Glans, L.I. Johansson, T. Balasubramanian, R.J. Blake, Phys. Rev. B 70 (2004) 033408.
[131] S.J. Tang, J. Shi, B. Wu, P.T. Sprunger, W.L. Yang, V. Brouet, X.J. Zhou, Z. Hussain, Z.-X. Shen, Z. Zhang, E.W. Plummer, Phys. Status Solidi b 241 (2004) 2345.
[132] J. Shi, S.-J. Tang, W. Biao, P.T. Sprunger, W.L. Yang, V. Brouet, X.J. Zhou, Z. Hussain, Z.-X. Shen, Z. Zhenyu, E.W. Plummer, Phys. Rev. Lett. 92 (2004) 186401.
[133] S.-J. Tang, H.-T. Jeng, C.-S. Hsue, Ismail, P.T. Sprunger, E.W. Plummer, Phys. Rev. B 77 (2008) 045405.
[134] K.B. Ray, J.B. Hannon, E.W. Plummer, Chem. Phys. Lett. 171 (1990) 469.
[135] V. Lossev, J. Küppers, J. Nucl. Mater. 196–198 (1992) 953.
[136] V. Lossev, J. Küppers, Surf. Sci. 284 (1993) 175.
[137] K.B. Ray, X. Pan, E.W. Plummer, Surf. Sci. 285 (1993) 66.
[138] P.J. Feibelman, Phys. Rev. B 48 (1993) 11270.
[139] R. Stumpf, P.J. Feibelman, Surf. Sci. 51 (1995) 13748.
[140] K. Pohl, E.W. Plummer, Surf. Sci. 59 (1999) R5324.
[141] K. Pohl, E.W. Plummer, S.V. Hoffmann, P. Hofmann, Phys. Rev. B 70 (2004) 235424.
[142] A. Allouche, Phys. Rev. B 78 (2008) 085429.
[143] C. Nieswand, M. Born, J. Hackmann, Plasma Phys. Control. Fusion 32 (1990) 197.
[144] P.K. Mioduszewski, P.H. Edmonds, C.E. Bush, A. Carnevali, R.E. Clausing, T.B. Cook, L.C. Emerson, A.C. England, W.A. Gabbard, L. Heatherly, D.P. Hutchinson, R.C. Isler, R.R. Kindsfather, P.W. King, R.A. Langley, E.A. Lazarus, C.H. Ma, M. Murakami, G.H. Neilson, J.B. Roberto, J.E. Simpkins, C.E. Thomas, A.J. Wootton, K. Yokoyama, R.A. Zuhr, K.H. Behringer, J. Dietz, E. Källne, P.J. Lomas, P.D. Morgan, P.E. Stott, A. Tanga, K.H. Sonnenberg, M.F. Smith, J. Watkins, R.D. Watson, J.B. Whitley, D.H.J. Goodall, N.J. Peacock, R. Clayton, J. von Seggern, K.G. Tschersich, Nucl. Fusion 26 (1986) 1171.
[145] ORMAK-ISX Group, Nucl. Fusion 25 (1985) 1127.
[146] J.P. Coad, M. Rubel, J. Likonen, Fusion Eng. Des. 138 (2018) 78.
[147] J. Wesson, Tokamaks, fourth ed., Oxford Science Publications, Oxford, United Kingdom, 2011.
[148] S. Brezinsek, A. Widdowson, M. Mayer, V. Philipps, P. Baron-Wiechec, J.W. Coenen, K. Heinola, A. Huber, J. Likonen, P. Petersson, M. Rubel, M.F. Stamp, D. Borodin, J.P. Coad, A.G. Carrasco, A. Kirschner, S. Krat, K. Krieger, B. Lipschultz, Ch. Linsmeier, G.F. Matthews, K. Schmid, Nucl. Fusion 55 (2015) 063021.
[149] G. De Temmerman, M.J. Baldwin, R.P. Doerner, Nucl. Fusion 48 (2008) 075008.
[150] Ch. Strupp, Ann. Occup. Hyg. 55 (2010) 43.
[151] A. Widdowson, A. Baron-Wiechec, J.P. Coad, K. Heinola, J. Likonen, C. Lungu, G.F. Matthews, M. Rubel, Phys. Scr. T 167 (2016) 014057.
[152] C.B.A. Forty, R.A. Forrest, G.J. Butterworth, J. Nucl. Mater. 258 (1998) 793.
[153] A.R. Raffray, B. Calcagno, P. Chappuis, Z. Fu, A. Furmanek, C. Jiming, D.-H. Kim, S. Khomiakov, A. Labusov, A. Martin, M. Merola, R. Mitteau, S. Sadakov, M. Ulrickson, F. Zacchia, Nucl. Fusion 54 (2014) 033004.
[154] ITER - Final Design Report, in: ITER EDA Documentation Series, vol. 16, 1998.
[155] G.F. Matthews, P. Edwards, T. Hirai, M. Kear, A. Lioure, P. Lomas, A. Loving, C. Lungu, H. Maier, P. Mertens, D. Neilson, R. Neu, J. Pamela, V. Philipps, G. Piazza, V. Riccardo, M. Rubel, C. Ruset, E. Villedieu, M. Way, Phys. Scr. T 128 (2007) 137.
[156] R. Mitteau, B. Calcagno, P. Chappuis, R. Eaton, S. Gicquel, J. Chen, A. Labusov, A. Martin, M. Merola, R. Raffray, M. Ulrickson, F. Zacchia, Fusion Eng. Des. 88 (2013) 568.
[157] M.-H. Aumenier, M. Kocan, R. Reichle, E. Gauthier, Nucl. Mater. Energy 12 (2017) 1265.
[158] R.A. Pitts, S. Carpentier, F. Escourbiac, T. Hirai, V. Komarov, A.S. Kukushkin, S. Lisgo, A. Loarte, M. Merola, R. Mitteau, A.R. Raffray, M. Shimada, P.C. Stangeby, J. Nucl. Mater. 415 (2011) S957.
[159] S. Lisgo, A. Kukushkin, R.A. Pitts, D. Reiter, J. Nucl. Mater. 438 (2013) 580.
[160] A. Khan, G. De Temmerman, S.W. Lisgo, X. Bonnin, H. Anand, M.A. Miller, R.A. Pitts, K. Schmid, A.S. Kukushkin, Nucl. Mater. Energy 20 (2019) 100674.
[161] J. Romazanov, S. Brezinsek, A. Kirschner, D. Borodin, A. Eksaeva, Richard A. Pitts, S.W. Lisgo, H. Anand, E. Veshchev, V.S. Neverov, A.B. Kukushkin, A.G. Alekseev, Ch. Linsmeier, Contrib. Plasma Phys. 60 (2020) 201900149.
[162] S. Carpentier, R.A. Pitts, P.C. Stangeby, J.D. Elder, A.S. Kukushkin, S. Lisgo, W. Fundamenski, D. Moulton, J. Nucl. Mater. 415 (2011) S165.
[163] K. Schmid, K. Krieger, S.W. Lisgo, et al., Nucl. Fusion 55 (2015) 053015.
[164] J. Romazanov, S. Brezinsek, D. Borodin, M. Groth, S. Wiesen, A. Kirschner, A. Huber, A. Widdowson, M. Airila, A. Eksaeva, I. Borodkina, Ch. Linsmeier, Nucl. Mater. Energy 18 (2019) 331.
[165] M. Kocan, R.A. Pitts, S.W. Lisgo, A. Loarte, J.P. Gunn, V. Fuchs, J. Nucl. Mater. 463 (2015) 709.
[166] A. Loarte, G. Huijsmans, S. Futatani, L.R. Baylor, T.E. Evans, D.M. Orlov, O. Schmitz, M. Becoulet, P. Cahyna, Y. Gribov, A. Kavin, A. Sashala Naik, D.J. Campbell, T. Casper, E. Daly, H. Frerichs, A. Kischner, R. Laengner, S. Lisgo, R.A. Pitts, G. Saibene, A. Wingen, Nucl. Fusion 54 (2014) 033007.
[167] B. Spilker, J. Linke, Th. Loewenhoff, G. Pintsuk, M. Wirtz, Nucl. Mater. Energy 12 (2017) 1184.

[168] M. Lehnen, K. Aleynikova, P.B. Aleynikov, D.J. Campbell, P. Drewelow, N.W. Eidietis, Yu. Gasparyan, R.S. Granetz, Y. Gribov, N. Hartmann, E.M. Hollmann, V.A. Izzo, S. Jachmich, S.-H. Kim, M. Kocan, H.R. Koslowski, D. Kovalenko, U. Kruezi, A. Loarte, S. Maruyama, G.F. Matthews, P.B. Parks, G. Pautasso, R.A. Pitts, C. Reux, V. Riccardo, R. Roccella, J.A. Snipes, A.J. Thornton, P.C. de Vries, J. Nucl. Mater. 463 (2015) 39.
[169] I. Jepu, G.F. Matthews, A. Widdowson, M. Rubel, E. Fortuna-Zalesna, J. Zdunek, P. Petersson, V.K. Thompson, P. Dinca, C. Porosnicu, P. Coad, K. Heinola, N. Catarino, O.G. Pompilian, C.P. Lungu, Nucl. Fusion 59 (2019) 086009.
[170] J. Coburn, E. Thoren, R.A. Pitts, H. Anand, M. Lehnen, L. Kos, M. Brank, S. Ratynskaia, P. Tolias, Phys. Scr. T 171 (2019) 014076.
[171] I. Bykov, H. Bergsåker, P. Petersson, J. Likonen, G. Possnert, Nucl. Instrum. Methods Phys. Res. B 332 (2014) 280.
[172] P.K. Khabibullaev, B.G. Skorodumov, Determination of Hydrogen in Materials - Nuclear Physics Methods, Springer-Verlag, Berlin Heidelberg, Germany, 1989.
[173] S. Krat, M. Mayer, C. Porosnicu, Nucl. Instrum. Methods Phys. Res. B 358 (2015) 72.
[174] N. Catarino, N.P. Barradas, E. Alves, Nucl. Instrum. Methods Phys. Res. B 371 (2016) 50.
[175] P. Tsavalas, A. Lagoyannis, K. Mergia, E. Ntemou, C.P. Lungu, Nucl. Instrum. Methods Phys. Res. B 479 (2020) 205.
[176] M. Oberkofler, R. Piechoczek, Ch. Linsmeier, Phys. Scr. T 145 (2011) 014011.
[177] J.P. Coad, M. Rubel, C.H. Wu, J. Nucl. Mater. 241–243 (1997) 408.
[178] I. Bykov, P. Petersson, H. Bergsåker, A. Hallén, G. Possnert, Nucl. Instrum. Methods Phys. Res. B 273 (2012) 250.
[179] B.L. Doyle, P.S. Peercy, Appl. Phys. Lett. 34 (1979) 811.
[180] A. Turos, O. Meyer, Nucl. Instrum. Methods Phys. Res. B 4 (1984) 92.
[181] C.R. Gossett, Nucl. Instrum. Methods Phys. Res. B 15 (1986) 481.
[182] J.A. Sawicki, Nucl. Instrum. Methods Phys. Res. B 23 (1987) 521.
[183] M. Friedrich, W. Pilz, G. Sun, R.-D. Penzhorn, N. Bekris, R. Behrisch, C. Garcia-Rosales, Phys. Scr. T 94 (2001) 98.
[184] A. Zaloznik, P. Pelicon, Z. Rupnik, I. Cadez, S. Markelj, Nucl. Instrum. Methods Phys. Res. B 371 (2016) 167.
[185] K. Schmid, U. von Toussaint, Nucl. Instrum. Methods Phys. Res. B 281 (2012) 64.
[186] S. Bielesch, M. Oberkofler, H.-W. Becker, H. Maier, D. Rogalla, T. Schwarz-Selinger, Ch. Linsmeier, Nucl. Instrum. Methods Phys. Res. B 317 (2013) 121.
[187] N.P. Barradas, C. Jeynes, Nucl. Instrum. Methods Phys. Res. B 266 (2008) 1875.
[188] N.P. Barradas, J. Likonen, E. Alves, L.C. Alves, P. Coad, A. Hakola, A. Widdowson, Nucl. Fusion 1336 (2010) 281.
[189] A. Baron-Wiechec, A. Widdowson, E. Alves, C.F. Ayres, N.P. Barradas, S. Brezinsek, J.P. Coad, N. Catarino, K. Heinola, J. Likonen, G.F. Matthews, M. Mayer, P. Petersson, M. Rubel, W. van Renterghem, I. Uytdenhouwen, JET-EFDA Contributors, J. Nucl. Mater. 463 (2015) 157.
[190] N. Catarino, N.P. Barradas, V. Corregidor A. Widdowson, A. Baron-Wiechec J.P. Coad, K. Heinola M. Rubel, E. Alves, Nucl. Mater. Energy 12 (2017) 559.
[191] K. Heinola, A. Widdowson, J. Likonen, T. Ahlgren, E. Alves, C.F. Ayres, A. Baron-Wiechec, N. Barradas, S. Brezinsek, N. Catarino, P. Coad, C. Guillemaut, I. Jepu, S. Krat, A. Lahtinen, G.F. Matthews, M. Mayer, JET Contributors, Phys. Scr. T 170 (2017) 014063.
[192] A. Huber, B. Schweer, V. hilipps, N. Gierse, M. Zlobinski, S. Brezinsek, W. Biel, V. Kotov, R. eyte Gonzales, Ph. Mertens, U. Samm, Fusion Eng. Des. 86 (2011) 1336.
[193] J. Karhunen, A. Hakola, J. Likonen, A. Lissovski, M. Laan, P. Paris, JET EFDA Contributors, J. Nucl. Mater. 463 (2015) 931.
[194] J. Oelmann, N. Gierse, C. Li, S. Brezinsek, M. Zlobinski, B. Turan, S. Haas, C. Linsmeier, SAB 144 (2018) 38.
[195] M. Zlobinski, G. Sergienko, Y. Martynova, D. Matveev, B. Unterberg, S. Brezinsek, B. Spilker, D. Nicolai, M. Rasinski, S. Möller, Ch. Linsmeier, C.P. Lungu, C. Porosnicu, P. Dinca, G. De Temmerman, Nucl. Mater. Energy 19 (2019) 503.
[196] J.H. Yu, M.J. Baldwin, R.P. Doerner, R.A. Pitts, R.D. Smirnov, H.W. Xu, J. Nucl. Mater. 438 (2013) S1150.
[197] J.P. Biersack, W. Eckstein, Appl. Phys. A34 (1984) 73.
[198] W. Eckstein, Calculated Sputtering, Reflection and Range Values, IPP Report, IPP 9/132, Max-Plank-Institut für Plasmaphysik, 2002.
[199] P.C. Zalm, Radiat. Eff. Lett. 86 (1983) 29.
[200] J. Roth, W. Eckstein, J. Bohdansky, J. Nucl. Mater. 165 (1989) 199.
[201] J. Roth, W. Eckstein, M. Guseva, Fusion Eng. Des. 37 (2002) 465.
[202] D.M. Mattox, D.J. Sharp, J. Nucl. Mater. 80 (1979) 115.
[203] M. Küstner, W. Eckstein, E. Hechtl, J. Roth, J. Nucl. Mater. 265 (1999) 22.
[204] R. Behrisch, W. Eckstein (Eds.), Sputtering by Particle Bombardment, Springer-Verlag, Berlin, 2007.
[205] R.P. Doerner, C. Björkas, D. Nishijima, T. Schwarz-Selinger, J. Nucl. Mater. 438 (2013) S272.
[206] E.M. Hollmann, A.Yu. Pigarov, Phys. Plasmas 9 (2002) 4330.
[207] D. Nishijima, R.P. Doerner, M.J. Baldwin, G. De Temmermann, J. Nucl. Mater. 390–391 (2009) 132.
[208] R.A. Causey, D. Walsh, J. Nucl. Mater. 254 (1998) 84.
[209] R.A. Causey, Private communication.
[210] R.P. Doerner, A. Grossman, S. Luckhardt, R. Seraydarian, F.C. Sze, D.G. Whyte, R.W. Conn, J. Nucl. Mater. 257 (1998) 51.
[211] R.P. Doerner, Scr. Mater. 143 (2018) 137.
[212] D. Borodin, M.F. Stamp, A. Kirschner, C. Björkas, S. Brezinsek, J. Miettunen, D. Matveev, C. Silva, O. Van Hoey, M. Groth, S. Marsen, V. Philipps, J. Nucl. Mater. 438 (2013) S267.
[213] S. Brezinsek, M.F. Stamp, D. Nishijima, D. Borodin, S. Devaux, K. Krieger, S. Marsen, M. O'Mullane, C. Björkas, A. Kirschner, JET EFDA Contributors, Nucl. Fusion 54 (2014) 103001.
[214] K. Nordlund, C. Björkas, K. Vörtler, A. Meinander, A. Lasa, M. Mehine, A.V. Krasheninnikov, Nucl. Instrum. Methods Phys. Res. B 269 (2011) 1257.
[215] G. Duxbury, M.F. Stamp, H.P. Summers, Plasma Phys. Control. Fusion 40 (1998) 361.
[216] D. Nishijima, R.P. Doerner, M.J. Baldwin, G. De Temmerman, E.M. Hollmann, Plasma Phys. Control. Fusion 50 (2008) 125007.
[217] R.P. Doerner, M.J. Baldwin, D. Buchenauer, G. De Temmerman, D. Nishijima, J. Nucl. Mater. 930–391 (2009) 681.
[218] C. Björkas, K. Vörtler, K. Nordlund, D. Nishijima, R. Doerner, New J. Phys. 11 (2009) 123017.
[219] R.A. Anderl, R.A. Causey, J.W. Davis, R.P. Doerner, G. Federici, A.A. Haasz, G.R. Longhurst, W.R. Wampler, K.L. Wilson, J. Nucl. Mater. 273 (1999) 1.
[220] R.P. Doerner, A.A. Grossman, S. Luckhardt, R. Seraydarian, F.C. Sze, D.G. Whyte, J. Nucl. Mater. 266–269 (1999) 392.
[221] J. Roth, E. Tsitrone, T. Loarer, V. Philipps, S. Brezinsek, A. Loarte, G.F. Counsell, R.P. Doerner, K. Schmid, O.V. Ogorodnikova, Plasma Phys. Control. Fusion 50 (2008) 103001.
[222] K. Heinola, J. Likonen, T. Ahlgren, S. Brezinsek, G. De Temmerman, I. Jepu, G.F. Matthews, R.A. Pitts, A. Widdowson, JET Contributors, Nucl. Fusion 57 (2017) 086024.
[223] G. De Temmerman, M.J. Baldwin, A. Anthoine, I. Jepu, J. Likonen, C.P. Lungu, C. Porosnicu, R.A. Pitts, K. Heinola, A. Jan, Nucl. Mater. Energy 12 (2017) 267.
[224] G. Counsell, P. Coad, C. Grisola, C. Hopf, W. Jacob, A. Kirschner, A. Kreter, K. Krieger, J. Likonen, V. Philipps, J. Roth, M. Rubel, E. Salancon, F.L. Tabares, A. Widdowson, Plasma Phys. Control. Fusion 48 (2006) B 189.
[225] M.J. Baldwin, T. Schwarz-Selinger, R.P. Doerner, Nucl. Fusion 54 (2014) 073005.
[226] M.J. Baldwin, R.P. Doerner, Nucl. Fusion 54 (2014) 083032.
[227] M.J. Baldwin, R.P. Doerner, J. Nucl. Mater. 467 (2015) 383.
[228] M.J. Simmonds, M.J. Baldwin, G. De Temmerman, R.P. Doerner, Phys. Scr. T 171 (2020) 014043.
[229] M.J. Baldwin, T. Schwarz-Selinger, R.P. Doerner, Nucl. Mater. Energy 12 (2017) 678.
[230] A. Zaloznik, M.J. Baldwin, R.P. Doerner, et al., J. Nucl. Mater. 512 (2018) 25.
[231] D. Alegre, M.J. Baldwin, M. Simmonds, et al., Phys. Scr. T 170 (2017) 014028.
[232] M. Miyamoto, D. Nishijima, M.J. Baldwin, et al., Nucl. Mater. Energy 12 (2017) 633.
[233] M. Tokitani, M. Miyamoto, S. Masuzaki, et al., Fusion Eng. Des. 116 (2017) 1.
[234] S. Masuzaki, M. Tokitani, T. Otsuka, et al., Phys. Scr. T 170 (2017) 014031.
[235] K. Sugiyama, J. Roth, A. Anghel, C. Porosnicu, M. Baldwin, R. Doerner, K. Krieger, C.P. Lungu, J. Nucl. Mater. 415 (2011) S731.
[236] K. Sugiyama, C. Porosnicu, W. Jacob, J. Roth, Th. Dürbeck, I. Jepu, C.P. Lungu, J. Nucl. Mater. 438 (2013) S1113.
[237] K. Sugiyama, C. Porosnicu, W. Jacob, I. Jepu, C.P. Lungu, Nucl. Mater. Energy 6 (2016) 1.
[238] C.P. Lungu, I. Mustata, V. Zaroschi, A.M. Lungu, A. Anghel, P. Chiru, M. Rubel, P. Coad, G.F. Matthews, Phys. Scr. T 128 (2007) 157.
[239] A. Marcu, C.M. Ticos, C. Grigoriu, I. Jepu, C. Porosnicu, A.M. Lungu, C.P. Lungu, Thin Solid Films 519 (2009) 4074.
[240] R.P. Doerner, M.J. Baldwin, G. De Temmerman, J. Hanna, D. Nishijima, J. Roth, K. Schmid, G.R. Tynan, K. Umstadter, Nucl. Fusion 49 (2009) 035002.
[241] J. Roth, T. Schwarz-Selinger, V. Kh. Alimov, E. Markina, J. Nucl. Mater. 432 (2013) 341.
[242] T. Vuoriheimo, P. Jalkanen, A. Liski, K. Mizohata, T. Ahlgren, K. Heinola, J. Räisänen, Phys. Scr. T 171 (2020) 014056.
[243] J.L. Barton, Y.Q. Wang, T. Schwarz-Selinger, R.P. Doerner, G.R. Tynan, J. Nucl. Mater. 438 (2013) S1138.
[244] D. Kogut, D. Douai, M.J. Baldwin, R.P. Doerner, D. Sinelnikov, N. Mamedov, V. Kurnaev, H.W. Becker, T. Schwarz-Selinger, Phys. Scr. T 167 (2016) 014062.
[245] T. Loarer, S. Brezinsek, V. Philipps, S. Romanelli-Gruenhagen, D. Alves, I. Carvalho, R. Felton, D. Douai, H.G. Esser, D. Frigione, Nucl. Fusion 55 (2015) 043021.
[246] T. Wauters, D. Douai, D. Kogut, A. Lyssoivan, S. Brezinsek, E. Belonohy, T. Blackman, V. Bobkov, K. Crombé, A. Drenik, M. Graham, E. Joffrin, E. Lerche, T. Loarer, P.L. Lomas, M.-L. Mayoral, I. Monakhov, M. Oberkofler, V. Philipps, V. Plyusnin, G. Sergienko, D. Van Eester, J. Nucl. Mater. 463 (2015) 1104.
[247] A. Widdowson, J.P. Coad, E. Alves, A. Baron-Wiechec, N.P. Barradas, S. Brezinsek, N. Catarino, V. Corregidor, K. Heinola, S. Koivuranta, S. Krat, A. Lahtinen, J. Likonen, G.F. Matthews, M. Mayer, P. Petersson, M. Rubel, Nucl. Fusion 57 (2017) 086045.

[248] ADAS - Atomic Data and Analysis Structure software package, http://www.adas.ac.uk.
[249] A. Kirschner, V. Philipps, J. Winter, U. Kögler, Nucl. Fusion 40 (2000) 989.
[250] D. Borodin, A. Kirschner, A. Kreter, V. Philipps, A. Pospieszczyk, R. Ding, R. Doerner, D. Nishijima, J. Yu, J. Nucl. Mater. 390 (2009) 106.
[251] D. Borodin, Private communication.
[252] D. Borodin, D. Nishijima, R.P. Doerner, S. Brezinsek, A. Kreter, A. Kirschner, J. Romazanov, I. Borodkina, A. Eksaeva, E. Marenkov, Ch. Linsmeier, Nucl. Mater. Energy 12 (2017) 1157.
[253] K.H. Behringer, J. Nucl. Mater. 145–147 (1987) 145.
[254] A. Pospieszczyk, D. Borodin, S. Brezinsek, A. Huber, A. Kirschner, Ph. Mertens, G. Sergienko, B. Schweer, I.L. Beigman, L. Vainshtein, J. Phys. B: At. Mol. Opt. Phys. 43 (2010) 144017.
[255] D. Nishijima, R.P. Doerner, R.P. Seraydarian, J. Nucl. Mater. 438 (2013) S1245.
[256] D. Nishijima, R.P. Doerner, D. Whyte, M.J. Baldwin, T. Schwarz-Selinger, J. Phys. B: At. Mol. Opt. Phys. 43 (2010) 225701.
[257] W. Eckstein, Calculated Sputtering, Reflection and Range Values, Report of the Max-Planck-Institute für PlasmaphysikIP, IP-Report 9/132, Garching, Germany, 2002.
[258] R.P. Doerner, D. Nishijima, T. Schwarz-Selinger, Phys. Scr. T 159 (2014) 014040.
[259] G.F. Matthews, JET-EFDA Contributors and ASDEX-Upgrade Team, J. Nucl. Mater. 438 (2013) S2.
[260] G.F. Matthews, S. Brezinsek, I. Chapman, J. Hobirk, L.D. Horton, C. Maggi, I. Nunes, F.G. Rimini, G. Sips, P. de Vries, Phys. Scr. T 159 (2014) 014015.
[261] S. Brezinsek, M.F. Stamp, D. Nishijima, D. Borodin, S. Devaux, K. Krieger, S. Marsen, M. O'Mullane, C. Björkas, A. Kirschner, Nucl. Fusion 54 (2014) 103001.
[262] X. Litaudon, EUROfusion Contributors, Nucl. Fusion 57 (2017) 102001.
[263] D. Nishijima, R.P. Doerner, M.J. Baldwin, G. De Temmerman, E.M. Hollmann, Plasma Phys. Control. Fusion 50 (2008) 125007.
[264] M. Rubel, P. Petersson, Y. Zhou, J.P. Coad, C. Lungu, I. Jepu, C. Porosnicu, D. Matveev, A. Kirschner, S. Brezinsek, A. Widdowson, E. Alves, Nucl. Fusion 57 (2017) 066027.
[265] P.R. Thomas, the JET Team, J. Nucl. Mater. 176–177 (1990) 3.
[266] M. Rubel, J.P. Coad, D.E. Hole, J. Nucl. Mater. 386–388 (2009) 729.
[267] M. Rubel, J.P. Coad, R.A. Pitts, J. Nucl. Mater. 367–370 (2007) 1432.
[268] M. Rubel, J.P. Coad, P. Wienhold, G.F. Matthews, V. Philipps, M. Stamp, T. Tanabe, Phys. Scr. T 111 (2004) 112.
[269] H. Maier, T. Hirai, M. Rubel, R. Neu, Ph. Mertens, H. Greuner, Ch. Hopf, G.F. Matthews, O. Neubauer, G. Piazza, E. Gauthier, J. Likonen, R. Mitteau, G. Maddaluno, B. Riccardi, V. Philipps, C. Ruset, C.P. Lungu, I. Uytdenhouwen, Nucl. Fusion 47 (2007) 222.
[270] M. Rubel, V. Bailescu, J.P. Coad, T. Hirai, J. Likonen, J. Linke, C.P. Lungu, G.F. Matthews, L. Pedrick, V. Riccardo, P. Sundelin, E. Villedieu, J. Phys. Conf. Ser. 100 (2008) 062028.
[271] M. Rubel, J.P. Coad, A. Widdowson, G.F. Matthews, H.G. Esser, T. Hirai, J. Likonen, J. Linke, C.P. Lungu, M. Mayer, L. Pedrick, C. Ruset, J. Nucl. Mater. 438 (2013) S1204.
[272] K. Heinola, C.F. Ayres ands A. Baron-Wiechec, P. Coad, J. Likonen, G.F. Matthews, A. Widdowson, Phys. Scr. T 159 (2014) 014013.
[273] P. Coad, E. Alves, N.P. Barradas, A. Baron-Wiechec, N. Catarino, K. Heinola, J. Likonen, M. Mayer, G.F. Matthews, P. Petersson, A. Widdowson, Phys. Scr. T 159 (2014) 014012.
[274] J. Likonen, E. Alves, A. Baron-Wiechec, S. Brezinsek, J.P. Coad, A. Hakola, K. Heinola, S. Koivuranta, G.F. Matthews, P. Petersson, M. Rubel, C. Stan-Sion, A. Widdowson, Phys. Scr. T 159 (2014) 014016.
[275] P. Petersson, M. Rubel, H.G. Esser, J. Likonen, S. Koivuranta, A. Widdowson, J. Nucl. Mater. 463 (2015) 814.
[276] M. Mayer, S. Krat, W. Van Renterghem, A. Baron-Wiechec, S. Brezinsek, I. Bykov, P. Coad, Yu. Gasparyan, K. Heinola, J. Likonen, A. Pisarev, C. Ruset, G. de Saint-Aubin, A. Widdowson, Phys. Scr. T 167 (2016) 014051.
[277] M. Mayer, S. Krat, A. Baron-Wiechec, Yu. Gasparyan, K. Heinola, S. Koivuranta, J. Likonen, C. Ruset, G. de Saint-Aubin, A. Widdowson, Phys. Scr. T 170 (2017) 014058.
[278] A. Lagoyannis, P. Tsavalas, K. Mergia, G. Provatas, K. Triantou, E. Tsompopoulou, M. Rubel, P. Petersson, A. Widdowson, S. Harissopulos, T.J. Mertzimekis, Nucl. Fusion 57 (2017) 076027.
[279] S Krat, M. Mayer, A. Baron-Wiechec, S. Brezinsek, P. Coad, Yu. Gasparyan, K. Heinola, I. Jepu, J. Likonen, P. Petersson, C. Ruset, G. de Saint-Aubin, A Widdowson, Phys. Scr. T 171 (2020) 014059.
[280] Y. Oya, S. Masuzaki, M. Tokitani, K. Azuma, M. Oyaidzu, K. Isobe, N. Asakura, A. Widdowson, K. Heinola, S. Jachmich, M. Rubel, Fusion Eng. Des. 132 (2018) 24.
[281] S. Moon, P. Petersson, M. Rubel, A. Widdowson, A. Baron-Wiechec, E. Fortuna-Zalesna, E. Alves, Nucl. Mater. Energy 19 (2019) 59.
[282] D. Ivanova, M Rubel, A. Widdowson, P. Petersson, J. Likonen, L. Marot, E. Alves, A. Garcia-Carrasco, G. Pintsuk, Phys. Scr. T 159 (2014) 014011.
[283] M. Rubel, S. Moon, P. Petersson, A. Garcia-Carrasco, A. Hallén, A. Krawczynska, E. Fortuna-Zaleśna, M. Gilbert, T. Plociński A. Widdowson, Phys. Scr. T 170 (2017) 014061.
[284] P. Strom, P. Petersson, M. Rubel, E. Fortuna-Zaleśna, A. Widdowson, G. Sergienko, J. Nucl. Mater. 516 (2019) 202.
[285] N. Catarino, A. Widdowson, A. Baron-Wiechec, J.P. Coad, K. Heinola, M. Rubel, E. Alves, Phys. Scr. T 170 (2017) 014059.
[286] D. Borodin, S. Brezinsek, I. Borodkina, J. Romazanov, D. Matveev, A. Kirschner, A. Lasa, K. Nordlund, C. Björkas, M. Airila, J. Miettunen, M. Groth, M. Firdaouss, Nucl. Mater. Energy 9 (2016) 604.
[287] R. Behrisch, W. Eckstein, Top. Appl. Phys. 110 (2007) 33.
[288] I. Borodkina, D. Borodin, A. Kirschner, I.V. Tsvetkov, V.A. Kurnaev, M. Komm, R. Dejarnac, Contrib. Plasma Phys. 56 (2016) 640.
[289] D. Borodin, S. Brezinsek, J. Miettunen, M. Stamp, A. Kirschner, C. Björkas, M. Groth, S. Marsen, C. Silva, S.W. Lisgo, D. Matveev, M. Airila, V. Philipps, Phys. Scr. T 159 (2014) 014057.
[290] E. Safi, G. Valles, A. Lasa, K. Nordlund, J. Phys. D: Appl. Phys. 50 (2017) 204003.
[291] D. Borodin, J. Romazanov, R.A. Pitts, S.W. Lisgo, S. Brezinsek, I. Borodkina, A. Eksaeva, E. Safi, K. Nordlund, A. Kirschner, Ch. Linsmeier, Nucl. Mater. Energy 19 (2019) 510.
[292] IAEA Atomic, Molecular, and Plasma-Material Interaction database, https://amdis.iaea.org/databases.
[293] C. Klepper, D. Borodin, M. Groth, A. Lasa, M. Airila, V. Bobkov, L. Colas, P. Jacquet, A. Kirschner, A. Terra, T.M. Biewer, E. Delabie, C. Giroud, Phys. Scr. T 167 (2016) 014035.
[294] I. Borodkina, D. Borodin, S. Brezinsek, A. Kirschner, I.V. Tsvetkov, V.A. Kurnaev, V. Bobkov, C.C. Klepper, A. Lasa, C. Guillemaut, P. Jacquet, M.F. Stamp, C. Giroud, S. Silburn, I. Balboa, E. Solano, Nucl. Mater. Energy 12 (2017) 341.
[295] D. Borodin, A. Kirschner, S. Carpentier-Chouchana, R.A. Pitts, S. Lisgo, C. Björkas, P.C. Stangeby, J.D. Elder, A. Galonska, D. Matveev, V. Philipps, U. Samm, Phys. Scr. T 145 (2011) 014008.
[296] R. Flohr, C. Gillet, Physica B+C 104 (1981) 423.
[297] R. Doerner, C. Mays, Fusion Eng. Des. 37 (1997) 325.
[298] R. Doerner, Private communication.
[299] A.T. Peacock, J. Nucl. Mater. 266–269 (1999) 423.
[300] M. Rubel, A. Widdowson, J. Grzonka, E. Fortuna-Zalesna, S. Moon, P. Petersson, N. Ashikawa, N. Asakura, D. Hamaguchi, Y. Hatano, K. Isobe, S. Masuzaki, H. Kurotaki, Y. Oya, M. Oyaidzu, M. Tokitani, JET Contributors, Fusion Eng. Des. 136 (2018) 579.
[301] A. Baron-Wiechec, E. Fortuna, J. Grzonka, M. Rubel, A. Widdowson, C. Ayres, J.P. Coad, K. Heinola, G.F. Matthews, Nucl. Fusion 55 (2015) 113033.
[302] E. Fortuna-Zalesna, J. Grzonka, M. Rubel, A. Garcia-Carrasco, A. Widdowson, A. Baron-Wiechec, L. Ciupinski, Nucl. Mater. Energy 12 (2017) 582.
[303] E. Fortuna-Zalesna, J. Grzonka, M. Rubel, S. Moon, P. Petersson, A. Widdowson, T. Plocinski, Phys. Scr. T 170 (2017) 014038.
[304] A. Garcia-Carrasco, P. Petersson, M. Rubel, A. Widdowson, E. Fortuna-Zalesna, M. Brix, L. Marot, JET Contributors, Nucl. Mater. Energy 12 (2017) 506.
[305] M. Tokitani, M. Miyamoto, S. Masuzaki, R. Sakamoto, Y. Oya, Y. Hatano, T. Otsuka, M. Oyaidzu, H. Kurotaki, T. Suzuki, D. Hamaguchi, K. Isobe, N. Asakura, A. Widdowson, K. Heinola, M. Rubel, JET Contributors, Fusion Eng. Des. 136 (2018) 199.
[306] S. Fazinic, T. Tadic, M. Vuksic, M. Rubel, P. Petersson, E. Fortuna-Zalesna, A. Widdowson, Anal. Chem. 90 (2018) 5744.
[307] T. Otsuka, S. Masuzaki, N. Ashikawa, Y. Hatano, Y. Asakura, T. Suzuki, K. Isobe, T. Hayashi, M. Tokitani, Y. Oya, D. Hamaguchi, H. Kurotaki, R. Sakamoto, H. Tanigawa, M. Nakamichi, A. Widdowson, JET Contributors, Nucl. Mater. Energy 17 (2018) 279.
[308] N. Ashikawa, Y. Torikai, N. Asakura, A. Widdowson, M. Rubel, M. Hara, T. Otsuka, K. Heinola, Y. Hatano, K. Isobe, M. Oyaidzu, S. Masuzaki, T. Hayashi, A. Baron-Wiechec, JET Contributors, Nucl. Mater. Energy 22 (2020) 100673.
[309] A. Widdowson, E. Alves, C.F. Ayres, A. Baron-Wiechec, S. Brezinsek, J.P. Coad, K. Heinola, J. Likonen, G.F. Matthews, M. Rubel, JET-EFDA Contributors, Phys. Scr. T 159 (2014) 014010.
[310] M. Rubel, A. Widdowson, E. Fortuna-Zaleśna, C. Ayres, M. Berry, M. Burford, S. Collins, P. Macheta, Phys. Scr. T 171 (2020) 014048.
[311] M.G. Ganchenkova, V.A. Borodin, R.M. Nieminen, Phys. Rev. B 79 (2009) 134101.
[312] M.G. Ganchenkova, P.V. Vladimirov, V.A. Borodin, J. Nucl. Mater. 386–388 (2009) 79.
[313] A. Allouche, M. Oberkofler, M. Reinelt, Ch. Linsmeier, J. Phys. Chem. C 114 (2010) 3588.
[314] S.C. Middleburgh, R.W. Grimes, Acta Metall. 59 (2011) 7095.
[315] P. Zhang, J. Zhao, B. Wen, J. Phys.: Condens. Matter 24 (2012) 095004.
[316] P. Zhang, J. Zhao, B. Wen, J. Nucl. Mater. 423 (2012) 164.
[317] L. Ferry, F. Virot, Y. Ferro, D. Matveev, Ch. Linsmeier, M. Barrachin, J. Nucl. Mater. 524 (2019) 323.
[318] L. Ferry, F. Virot, M. Barrachin, Y. Ferro, C. Pardanaud, D. Matveev, M. Wensing, T. Dittmar, M. Koppen, C. Linsmeier, Nucl. Mater. Energy 12 (2017) 453.
[319] A. Allouche, N. Fernandez, Y. Ferro, J. Phys.: Condens. Matter 26 (2014) 315012.

[320] A. Allouche, Y. Ferro, Solid State Ion. 272 (2015) 91.
[321] A. Allouche, M. Oberkofler, M. Köppen, Ch. Linsmeier, Int. J. Hydrogen Energy 40 (2015) 16419.
[322] E. Safi, C. Björkas, A. Lasa, K. Nordlund, I. Sukuba, M. Probst, J. Nucl. Mater. 463 (2015) 805.
[323] M.J. Baldwin D. Nishijima, G. De Temmerman, J. Nucl. Mater. 390–391 (2009) 132–135.
[324] E. Safi, A. Zitting, K. Nordlund, Nucl. Mater. Energy 9 (2016) 571.
[325] D. Matveev, M. Wensing, L. Ferry, F. Virot, M. Barrachin, Y. Ferro, Ch. Linsmeier, Nucl. Instrum. Methods Phys. Res. B 430 (2018) 23.
[326] G.R. Longhurst, TMAP7: Tritium Migration Analysis Programme, in: INEEL/EXT-04-02352, Idaho National Laboratory, US, 2004.
[327] T. Ahlgren, K. Heinola, K. Vörtler, J. Keinonen, J. Nucl. Mater. 427 (2012) 152.
[328] K. Schmid, U. von Toussaint, T. Schwarz-Selinger, J. Appl. Phys. 116 (2014) 134901.
[329] E. Hodille, X. Bonnin, R. Bisson, T. Angot, C.S. Becquart, J.M. Layet, C. Grisolia, J. Nucl. Mater. 467 (2015) 424.
[330] R. Delaporte-Mathurin, E.A. Hodille, J. Mougenot, Y. Charles, C. Grisolia, Nucl. Mater. Energy 20 (2019) 100709.
[331] S. Benannoune, Y. Charles, J. Mougenot, M. Gaspérini, G. De Temmerman, Nucl. Mater. Energy 19 (2019) 42.
[332] M. Reinelt, A. Allouche, M. Oberkofler, Ch. Linsmeier, New J. Phys. 11 (2009) 043023.
[333] M. Oberkofler, M. Reinelt, Ch. Linsmeier, Nucl. Instrum. Methods Phys. Res. B 269 (2011) 1266.
[334] R. Piechoczek, M. Reinelt, M. Oberkofler, A. Allouche, Ch. Linsmeier, J. Nucl. Mater. 438 (2013) S1072.
[335] D. Matveev, M. Zlobinski, B. Unterberg G. De Temmerman, C. Linsmeier, Phys. Scr. T 171 (2020) 014053.
[336] M. Wensing, Reaction-Diffusion Modelling of Hydrogen Retention and Release Mechanisms in Beryllium (Master's thesis), Forschungszentrum Jülich, Germany, ISBN: 978-3-95806-184-2, 2016.
[337] G. Cambi, D.G. Cepraga, L. Di Pace, F. Druyts, V. Massaut, Fusion Eng. Des. 85 (2010) 1139.
[338] C. Makepeace, C. Pardanaud, P. Roubin, I. Borodkina, C. Ayres, P. Coad, A. Baron-Wiechec, I. Jepu, K. Heinola, A. Widdowson, S. Lozano-Perez, Nucl. Mater. Energy 19 (2019) 346.
[339] G. Pintsuk, S. Brezinsek, A. Huber, M. Rubel, A. Widdowson, Phys. Scr. T 171 (2020) 014042.
[340] J. Likonen, K. Heinola, A. De Backer, A. Baron-Wiechec, N. Catarino, I. Jepu, C.F. Ayres, P. Coad, S. Koivuranta, S. Krat, G.F. Matthews, M. Mayer, A. Widdowson, Nucl. Mater. Energy 19 (2019) 166.
[341] A. Widdowson, E. Alves, A. Baron-Wiechec, N.P. Barradas, N. Catarino, P. Coad, V. Corregidor, A. Garcia-Carrasco, K. Heinola, S. Koivuranta, S. Krat, A. Lahtinen, J. Likonen, M. Mayer, P. Petersson, M. Rubel, S. Van Boxel, Nucl. Mater. Energy 12 (2017) 499.
[342] P. Petersson, et al., Proc. 17th International Conference on Plasma-Facing Materials and Components, PFMC-17, Eindhoven, Netherlands, 2019.
[343] Y. Zayachuk, et al., Proc. 31st Symposium on Fusion Technology, SOFT2020, Dubrovnik, Croatia, submitted for publication, 2020.